

JGR Solid Earth



RESEARCH ARTICLE

10.1029/2023JB028065

Key Points:

- 3D microtomography images of sheared partially molten rocks reveal scale-dependent melt network properties
- The permeability parallel to melt-rich bands is similar to that of rocks with textural equilibrium melt geometries
- Melt cannot flow over long distances perpendicular to melt-rich band due to lack of melt connectivity in that direction and scale

Supporting Information:

Supporting Information may be found in the online version of this article.

Correspondence to:

J. Bader, jabader@terpmail.umd.edu

Citation:

Bader, J., Zhu, W., Montési, L., Qi, C., Cordonnier, B., Kohlstedt, D., & Warren, J. (2024). Effects of stress-driven melt segregation on melt orientation, melt connectivity and anisotropic permeability. *Journal of Geophysical Research: Solid Earth*, 129, e2023JB028065. https://doi.org/10.1029/2023JB028065

Received 18 OCT 2023 Accepted 14 FEB 2024

Author Contributions:

Conceptualization: James Bader.

Wenlu Zhu, Chao Qi, David Kohlstedt
Data curation: James Bader,
Laurent Montési
Formal analysis: James Bader,
Wenlu Zhu, Laurent Montési, Chao Qi
Funding acquisition: Wenlu Zhu
Investigation: James Bader, Wenlu Zhu,
Chao Qi

Methodology: James Bader, Wenlu Zhu, Laurent Montési, Chao Qi, Benoit Cordonnier, David Kohlstedt Project administration: Wenlu Zhu Software: James Bader, Wenlu Zhu, Laurent Montési

Supervision: Wenlu Zhu, Laurent Montési

© 2024 The Authors

This is an open access article under the terms of the Creative Commons Attribution-NonCommercial License, which permits use, distribution and reproduction in any medium, provided the original work is properly cited and is not used for commercial purposes.

Effects of Stress-Driven Melt Segregation on Melt Orientation, Melt Connectivity and Anisotropic Permeability

James Bader¹, Wenlu Zhu¹, Laurent Montési², Chao Qi², Benoit Cordonnier³, David Kohlstedt⁴, and Jessica Warren⁵

¹Department of Geology, University of Maryland, College Park, MD, USA, ²Institute of Geology and Geophysics, Chinese Academy of Sciences, Beijing, China, ³European Synchrotron Radiation Facility - 71, Grenoble Cedex 9, France, ⁴Department of Earth & Environmental Sciences, University of Minnesota, Minneapolis, MN, USA, ⁵Department of Earth Sciences, University of Delaware, Newark, DE, USA

Abstract Stress-driven melt segregation may have important geochemical and geophysical effects but remains a poorly understood process. Few constraints exist on the permeability and distribution of melt in deformed partially molten rocks. Here, we characterize the 3D melt network and resulting permeability of an experimentally deformed partially molten rock containing several melt-rich bands based on an X-ray microtomography data set. Melt fractions range from 0.08 to 0.28 in the ~20-μm-thick melt-rich bands, and from 0.02 to 0.07 in the intervening ~ 30 -µm-thick regions. We simulated melt flow through subvolumes extracted from the reconstructed rock at five length scales ranging from the grain scale (3 µm) to the minimum length required to fully encompass two melt-rich bands (64 µm). At grain scale, few subvolumes contain interconnected melt, and permeability is isotropic. As the length scale increases, more subvolumes contain melt that is interconnected parallel to the melt bands, but connectivity diminishes in the direction perpendicular to them. Even if melt is connected in all directions, permeability is lower perpendicular to the bands, in agreement with the elongation of melt pockets. Permeability parallel to the bands is proportional to melt fraction to the power of an exponent that increases from ~ 2 to 5 with increasing length scale. The permeability in directions parallel to the bands is comparable to that for an isotropic partially molten rock. However, no flow is possible perpendicular to the bands over distances similar to the band spacing. Melt connectivity limits sample scale melt flow to the plane of the melt-rich bands.

Plain Language Summary When a mixture of solid olivine grains and basaltic melt is subjected to differential stress, the melt can collect into sheet-like bands. Melt transport properties, including melt trajectories, chemical diffusion, and ductile creep, may all become anisotropic in the presence of these melt-rich bands. We present here the first quantification of the melt network properties in three dimensions based on synchrotron X-ray microtomography of experimentally deformed olivine/basalt aggregates. We show that the melt network presents no connection between melt-rich bands, restricting flow to the directions contained in the planes of these bands. Even at grain scale, melt pockets are preferentially oriented along the plane of the bands. The relationship between melt content and permeability derived from undeformed rocks is not valid at sample scale in sheared aggregates.

1. Introduction

The chemical and physical properties of partially molten regions of the upper mantle and lower crust are strongly influenced by the amount of melt present and, therefore, by the efficiency of magma segregation. Localized melt flow along high-permeability paths may explain trace-element and uranium series disequilibrium observed in mid-ocean ridge basalts (e.g., Jull et al., 2002; Liu & Liang, 2019). However, the origin of these paths is not yet certain. Previous experimental studies showed that melt in olivine-basalt rocks, selected as a chemically simple representation of the upper mantle, concentrates into sheet-like structures when subjected to stress (e.g., Holtzman et al., 2003; King et al., 2010, 2011; Qi et al., 2015, 2018; Qi & Kohlstedt, 2018). This behavior arises from porosity weakening and the feedback between melt content and deformability of a melt-rock aggregate (e.g., Katz et al., 2006; Stevenson, 1989). The physical properties of partially molten rocks, such as permeability and viscosity, are sensitive to the three-dimensional (3-D) melt topology (Kohlstedt & Holtzman, 2009). In an undeformed olivine basalt system, melt forms a homogeneously distributed, interconnected network along triple

BADER ET AL. 1 of 22

Validation: James Bader, Laurent Montési, Jessica Warren Visualization: James Bader, Laurent Montési, Benoit Cordonnier, Jessica Warren Writing - original draft: James Bader Writing - review & editing: James Bader, Wenlu Zhu, Laurent Montési, Chao Qi, Benoit Cordonnier, David Kohlstedt, Jessica Warren

junctions and grain boundaries (e.g., Zhu et al., 2011). Melt distribution, geometry, and associated transport are likely quite different in a sheared partially molten aggregate of the same composition, but these properties have not previously been quantified in three dimensions. Here, we use synchrotron X-ray microtomography to characterize the melt distribution and permeability of a deformed olivine-basalt aggregate containing discrete melt-

Small pockets of basaltic melt in an otherwise solid olivine aggregate become preferentially oriented 20°-30° antithetic to the shear plane when the aggregate is deformed in torsional shear experiments to strains greater than ~0.5 (Qi et al., 2015, 2018). Planar melt-rich bands, with a similar orientation, emerge at strains greater than ~1 (e.g., Holtzman et al., 2003; King et al., 2010, 2011; Qi et al., 2015, 2018; Qi & Kohlstedt, 2018; Zimmerman et al., 1999). This melt-preferred-orientation (MPO) could alter diffusion pathways, introduce viscous anisotropy (Takei & Holtzman, 2009a, 2009b), induce anisotropic permeability (Hier-Majumder, 2011), and change the power-law exponent of the permeability-melt fraction relationship from ~2 to ~3 due to melt flow being more sheet-like (Holtzman & Kohlstedt, 2007). Taylor-West and Katz (2015) suggested that the associated permeability anisotropy is responsible for the difference between the experimentally observed melt-rich band angle (20– 30°) and the theoretical prediction (i.e., 45°, Stevenson, 1989), although other phenomena such as a non-linear aggregate viscosity could also explain this observation (Katz et al., 2006).

Such heterogeneous melt distribution and anisotropic permeability would be in stark contrast to those in an undeformed rock, in which basaltic melt resides along the edges of olivine grains and permeability is isotropic (e.g., Cmíral et al., 1998; Connolly et al., 2009; Riley & Kohlstedt, 1991; von Bargen and Waff, 1986; Waff & Bulau, 1979; Wark & Watson, 1998; Zhu & Hirth, 2003). Indeed, high-resolution images of the 3-D melt distribution of undeformed, textually equilibrated partially molten aggregates revealed a homogeneous, wellconnected melt network for melt fractions from 0.02 to 0.20 (Zhu et al., 2011). Miller et al. (2014, 2016) found that the permeability in these samples is isotropic and can be described by a power-law function of melt fraction with an exponent of ~ 2.6 .

Stress-driven melt localization likely influences melt extraction and transport in the upper mantle (e.g., Katz et al., 2006, 2022), but these effects can only be studied if the 3-D melt distribution and permeability anisotropy of deformed partially molten rocks is well understood. Here, we use synchrotron X-ray microtomography (Zhu et al., 2011) to constrain the 3-D melt distribution of a partially molten sample containing several stress-driven melt-rich bands (Qi & Kohlstedt, 2018). Following a digital rock physics approach (Miller et al., 2014), we construct digital rocks based on the high-resolution 3-D data and characterize the orientation of the spaces where melt resides, called here melt volumes, as well as the total and connected melt fractions, permeability, and permeability anisotropy at different scales throughout the sample. We focus on changes in transport properties as a function of length scale and orientation with respect to the melt-rich bands. We compare the permeability-melt fraction relationship in this sheared partially molten rock to the one Miller et al. (2014) obtained for the textually equilibrated olivine-basalt aggregates. We also compare our results to prior permeability estimates for a deformed olivine-basalt sample (Holtzman et al., 2003). Our data provide the first systematic, quantitative analysis of the heterogeneous and anisotropic transport properties of experimentally produced partially molten olivine-basalt rocks containing shear-induced melt-rich bands. The results, including a complete lack of connection between adjacent melt-rich bands, provide important experimental constraints on melt transport under stress.

2. Experimental and Analytical Methods

2.1. Sample Description and Microtomographic Imaging

A homogenous mixture of fine-grained powders, comprising 90 vol% San Carlos olivine and 10 vol% mid-ocean ridge basalt, was hot-pressed to produce an olivine-basalt aggregate. After hot pressing, the aggregate was sheared in torsion using a Paterson apparatus at 1,200°C, hot enough for the basalt to be molten but the olivine to remain solid, under a confining pressure of 300 MPa, shear stress of 110 MPa, at a strain rate at the location where our sample was taken of $1.8 \times 10^{-4} \text{ s}^{-1}$ (Qi et al., 2018). After a shear strain of 13.3 was reached, the deformed aggregate was cooled rapidly to preserve its microstructure. Post-deformation optical and scanning electron microscopy revealed that the experimental charge developed distinct melt-rich bands and contained a sampleaverage melt fraction of ~0.06. The average grain size near the outer rim of the aggregate was ~3.1 μm (Qi et al., 2018).

BADER ET AL. 2 of 22

21699356, 2024, 3, Downloaded from https://agupubs.onlinelibrary.wiley.com/doi/10.1092/2023/B0828065 by Norwegian Institute Of Public Healt Invoice Receipt DFO, Wiley Online Library on [04.03/2024]. See the Terms and Conditions (https://onlinelibrary.wiley.com/terms-and-conditions

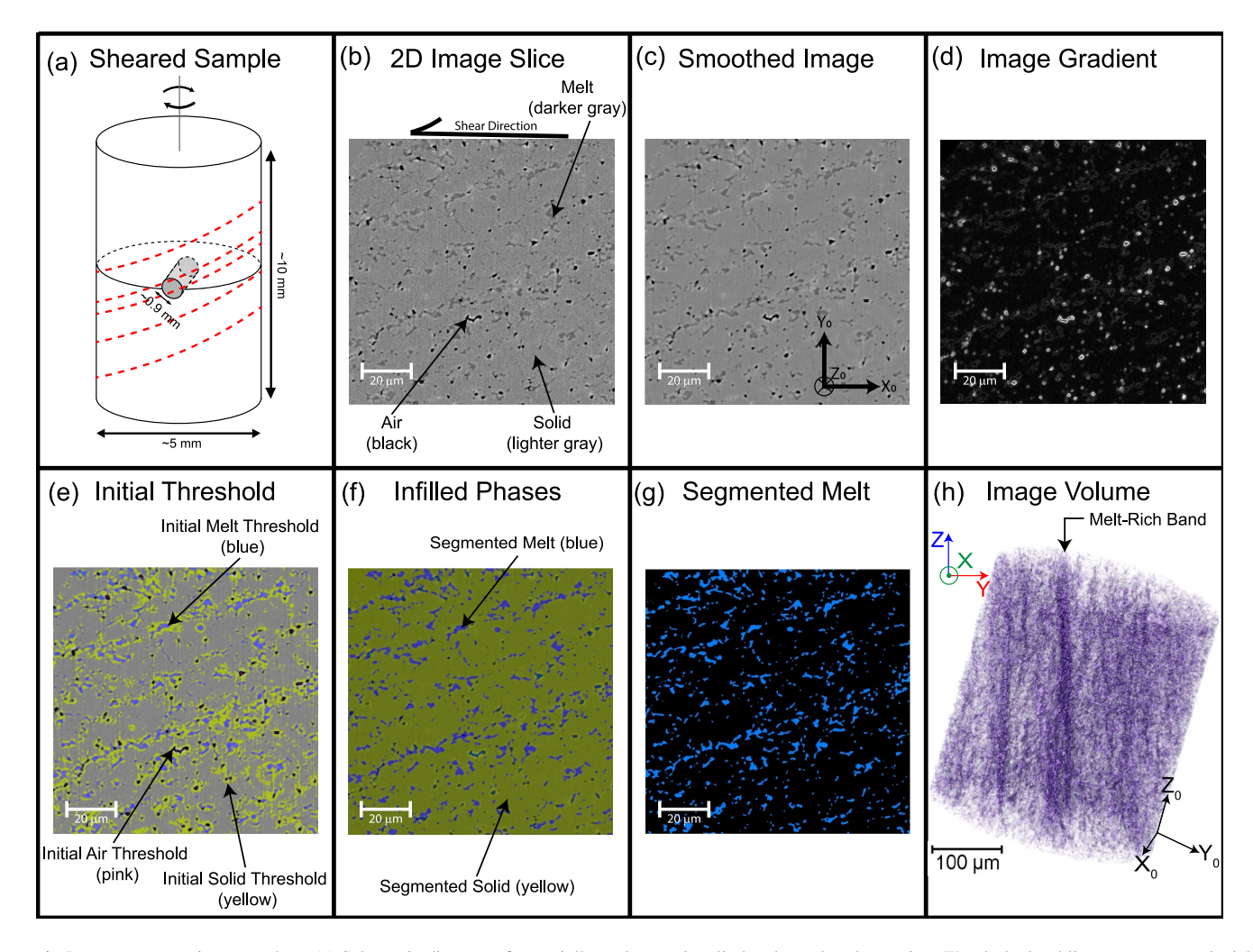


Figure 1. Image segmentation procedure. (a) Schematic diagram of a partially molten rock cylinder sheared under torsion. The dashed red lines represent melt-rich bands. The gray cylindrical core CQ0705 was imaged using synchrotron microtomography; (b) 2-D grayscale image of the reconstructed microtomography data. Olivine, melt, and air appear in medium gray, dark gray, and black, respectively; (c) Denoised 2-D grayscale image after an anisotropic diffusion filter was applied; (d) Map of grayscale gradient, where regions with high gradients (white) are identified as phase interfaces; (e) Initial infill areas for melt (blue), air (black) and olivine (yellow) into different "basins" bounded by the previously identified phase interfaces; (f) Inundation of watershed basins for both melt (blue) and non-melt (yellow); (g) Segmented binary image with each pixel labeled as either melt (blue) or non-melt (olivine and air, black); (h) 3-D visualization of the reconstructed digital rock with regions identified as melt shown in purple. The sample is rotated to highlight planar melt-rich bands (dark purple). The analysis coordinate system is defined with its X-Z plane parallel to the planar melt-rich bands and the Y direction normal to them, unlike the coordinate system for microtomographic reconstruction, X_0 , Y_0 , and Z_0 . Note that even though the segmentation was performed in 3-D, (b-g) shows a 2-D slice through the 3-D volume for ease of visualization.

A cylindrical core CQ0705 (\sim 0.9 mm diameter and length) was taken from the outer rim of the experimental charge, as illustrated in Figure 1a. This location experienced maximum shear strain and was chosen to ensure CQ0705 would contain well-developed melt-rich bands (Qi et al., 2018). The axis of CQ0705 is along the radial direction of the experimental charge (Figure 1a). Electron backscatter diffraction analysis of a thin section of the CQ0705 core yielded a grain size of 2.2–3.0 μ m (Bader, 2020). An average grain size of \sim 3 μ m is assumed, consistent with both Bader (2020) and Qi et al. (2018).

CQ0705 was imaged using synchrotron-based X-ray microtomography at the European Synchrotron Radiation Facility (ESRF). The core was rotated over 180° along its axis, and 1,800 radiographs were collected. Using this collection of radiographs, tomographic techniques were used to determine the variation in X-ray attenuation in 3-D throughout the imaged sample. When an X-ray passes through the sample, it is attenuated by different amounts based on the atomic number of the material it traverses. In general, denser materials absorb more photons than less dense ones. Therefore, minerals can be identified based on their X-ray absorption characteristics. Because the density difference between olivine and basalt is only $\sim 10\%$, phase contrast imaging techniques must be adopted to

BADER ET AL. 3 of 22

produce volumetric data in which these phases can be distinguished (Zhu et al., 2011). The reconstruction of the 3-D volumes from the radiographs was performed at beamline ID19 at the ESRF, using both X-ray absorption and phase contrast imaging (Mirone et al., 2014). In the reconstructed data set, different gray-scale values (Figure 1b) were assigned to each voxel (3-D pixel) according to the phase-contrast-enhanced X-ray absorption coefficients.

2.2. Image Processing

The reconstructed 3-D data set considered here as "the sample" is a cylindrical portion of CQ0705, with a height and a diameter of 328 μ m, that contains several melt-rich bands (Figure 1h). The side of each voxel within the 3-D data set is 0.16 μ m long. The grayscale value distribution of the 3-D data set is presented in the Figure S1 in Supporting Information S1. Figure 1b shows a representative two-dimensional (2-D) slice of the 3-D data set. Voids (air), the least dense materials, appear black, basalt appears dark gray, and olivine, the densest phase, appears light gray. The reconstruction of the 3-D data set was performed in a coordinate system (X_0 , Y_0 , Z_0), where the Z_0 -axis is the rotation axis of the sample during the microtomographic scan (Figure 1c).

Phase contrast imaging tends to produce artifacts along the interfaces between two different phases (Figure 1b). Noise reduction was performed before image segmentation to remove these artifacts. Following Miller et al. (2014), we applied the *Anisotropic Diffusion* filter (Weickert, 1999), which is available in the Avizo (©ThermoFisher Scientific) image filter library. This filter removes small, sudden fluctuations of the grayscale value. The denoised image is smoother and mostly free of artifacts (Figure 1c). A comparison of the grayscale between the denoised image and the original one is shown in the Figure S2 in Supporting Information S1.

We segmented the denoised microtomographic data set to identify which voxels (3-D pixels) correspond to the various phases present in the sample. As in Miller et al. (2014), we found that the best segmentation method for this data set is the so-called *Watershed* algorithm (Ohser & Schladitz, 2009, p. 325). Segmentation yielded a melt fraction of ~0.078 of the entire sample, in good agreement with the estimate reported by Qi et al. (2018). The workflow of image segmentation is described here and in Figure 1.

To segment each phase using the watershed algorithm, the first step is to calculate the grayscale-gradient magnitude (Miller et al., 2014). High magnitude gradients (i.e., large differences in grayscale value between neighboring pixels, see Text S1 in Supporting Information S1 for an example and explanation) suggest that there is a change in phase, that is, an interface between different phases. Using the calculated gradient magnitudes, we identified each interface between melt and olivine, melt and air, or olivine and air (Figure 1d). Next, we filled the "basins" delineated by the interfaces with the corresponding phase. After experimentation, we selected threshold values appropriate to identify for each phase (melt, olivine, or air, see Figure S2 in Supporting Information S1). The result of the initial infill is shown in Figure 1e. Because this study focuses on transport properties, in the final step of segmentation, we inundated the melt basins and merged the non-melt (olivine + air) basins (Figure 1f) to produce a binary representation of the sample, where the values 1 and 0 correspond to melt and non-melt (Figure 1g), respectively. The result of this segmentation procedure is a 3-D digital rock with clearly identified melt (Figure 1h).

To quantify the effect of stress-driven melt-rich bands on the anisotropic transport behavior, we define a coordinate system (X, Y, Z) in which the X-Z plane is parallel to the planar melt-rich bands, and the Y-axis is normal to the melt-rich bands (Figure 1h). To align the sample, a rotation of 344° around the X_0 -axis and 20° around the Z_0 -axis was applied.

Melt-rich bands typically form at a $\sim 20-30^\circ$ angle to the shear direction in experiments. In samples deformed in torsion, band angles tend to fall toward the lower angle of this range (Holtzman et al., 2003; Qi et al., 2018). Thus, the direction of the maximum compressive stress can be inferred to be approximately -70° from the *Y*-axis of the rotated sample. The shear direction is within the X_0 – Y_0 plane, and determined by the melt-rich band orientation (Figure 1b).

2.3. Systematic Subvolume Selection

Partially molten rocks with discrete melt-rich bands are heterogeneous. As we will demonstrate, their transport properties are scale-dependent. To quantify heterogeneity, we discretized the digital rock into equal-sized cubic subvolumes (Figure 2a) and calculated the transport properties of each subvolume. To address the scale dependence, we compared the results from subvolumes of five different sizes. The smallest subvolumes have

BADER ET AL. 4 of 22

21699356, 2024, 3, Downloaded from https://agupubs.onlinelibtary.wiley.com/doi/10.1029/2023JB028065 by Norwegian Institute Of Public Healt Invoice Receipt DFO, Wiley Online Library on [0.403/2024]. See the Terms and Conditions (https://agupubs.onlinelibrary.wiley.com/doi/10.1029/2023JB028065 by Norwegian Institute Of Public Healt Invoice Receipt DFO, Wiley Online Library on [0.403/2024]. See the Terms and Conditions (https://agupubs.onlinelibrary.wiley.com/doi/10.1029/2023JB028065 by Norwegian Institute Of Public Healt Invoice Receipt DFO, Wiley Online Library on [0.403/2024]. See the Terms and Conditions (https://agupubs.onlinelibrary.wiley.com/doi/10.1029/2023JB028065 by Norwegian Institute Of Public Healt Invoice Receipt DFO, Wiley Online Library on [0.403/2024]. See the Terms and Conditions (https://agupubs.com/doi/10.1029/2023JB028065 by Norwegian Institute Of Public Healt Invoice Receipt DFO, Wiley Online Library on [0.403/2024]. See the Terms and Conditions (https://agupubs.com/doi/10.1029/2023JB028065 by Norwegian Institute Of Public Healt Invoice Receipt DFO, Wiley Online Library on [0.403/2024]. See the Terms and Conditions (https://agupubs.com/doi/10.1029/2023JB028065 by Norwegian Institute Of Public Healt Invoice Receipt DFO, Wiley Online Library on [0.403/2024]. See the Terms and Conditions (https://agupubs.com/doi/10.1029/2023JB028065 by Norwegian Institute Of Public Healt Invoice Receipt DFO, Wiley Online Library on [0.403/2024]. See the Terms and Conditions (https://agupubs.com/doi/10.1029/2023JB028065 by Norwegian Institute Of Public Healt Invoice Receipt DFO, Wiley Online Library on [0.403/2024]. See the Terms and Conditions (https://agupubs.com/doi/10.1029/2023JB028065 by Norwegian Institute Of Public Healt Invoice Receipt DFO, Wiley Online Library on [0.403/2024]. See the Terms and Conditions (https://agupubs.com/doi/10.1029/2023JB028065 by Norwegian Institute Of Public Healt Invoice Receipt DFO, Wiley Online Library on [0.403/2024]. See the Terms and Conditions (https://agupubs.com/doi/10.1

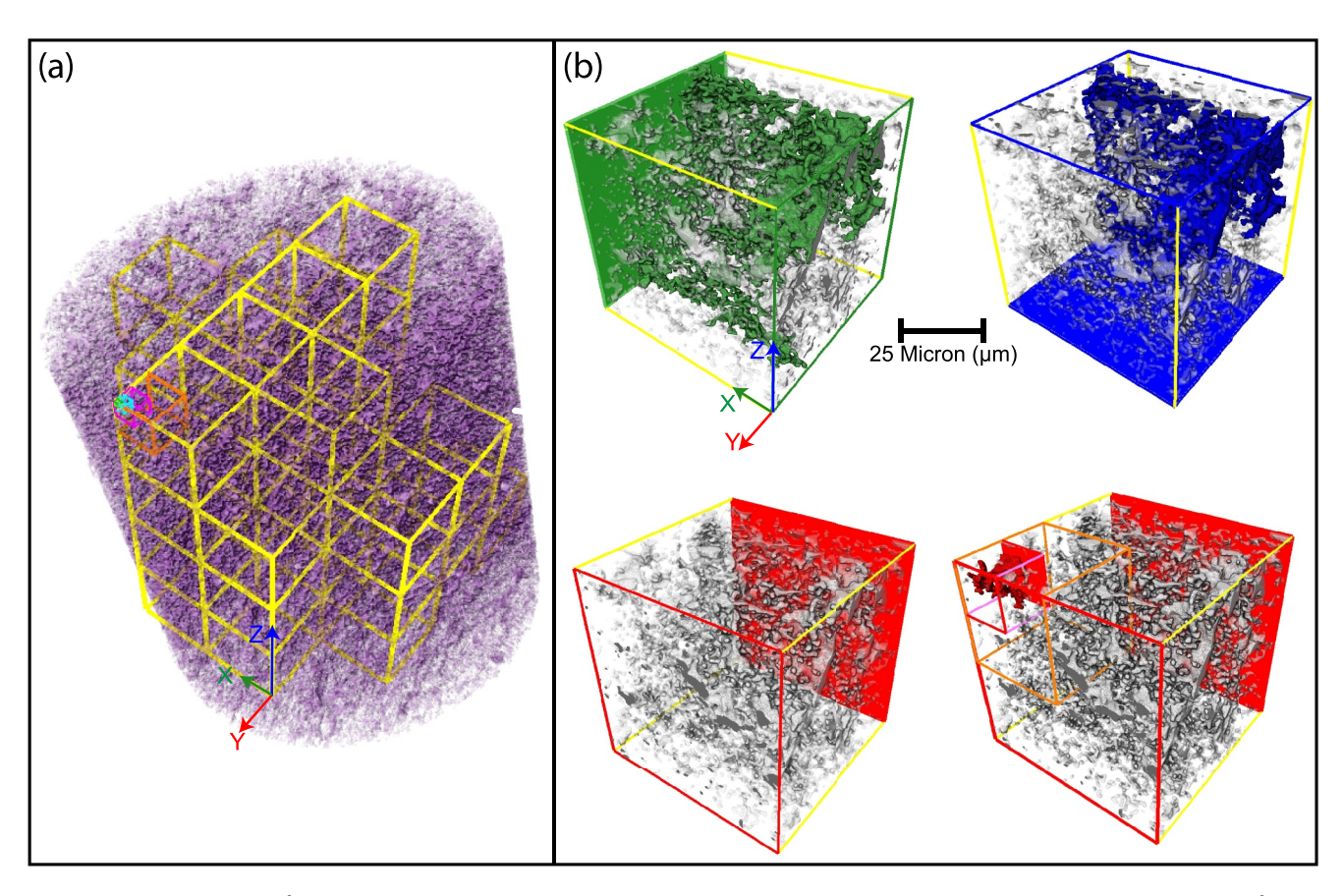


Figure 2. (a) The full set of 400-pixel³ subvolumes (yellow cubes) generated by discretizing the digital rock, with an inset of a 200-, 100-, 50-, and 20-pixel³ subvolume. (b) Interconnected melt networks in a single representative 400-pixel³ subvolume were calculated along the X-, Z-, and Y-directions (green, blue, and red, respectively). Disconnected melt voxels are shown in gray. See Section 2.4 for details. Although there is no interconnected melt network in the Y-direction over the 400-pixel³ subvolume (yellow cube), an interconnected melt network is detected in a 100-pixel³ subvolume at the upper left corner (pink cube). For comparison, a 200-pixel³ subvolume (orange cube) is also shown.

lengths of 20 pixels (\sim 3.2 µm), which is barely larger than the average grain size of \sim 3 µm (Bader, 2020; Qi et al., 2018). These 20-pixel³ subvolumes contain \sim 1 olivine grain each. We then defined additional sets of subvolumes with lengths of 50, 100, 200, and 400 pixels (or \sim 8, \sim 16, \sim 32, and \sim 64 µm), which contain \sim 20, \sim 100, \sim 1,000, and \sim 10,000 grains each, respectively. The planar melt-rich bands have a thickness of \sim 125 pixels (\sim 20 µm) and are separated by melt-poor regions \sim 250 pixels (\sim 40 µm) thick. Thus, the dimensions of the 100-pixel³ subvolumes are close to the scale of the melt-rich bands, and individual subvolumes of this size could be located entirely within one melt-rich or melt-poor region. The largest subvolumes at 400-pixel³ are large enough to always encompass both melt-rich and melt-poor regions. However, the proportions of these regions vary from one subvolume to another, as even these subvolumes are not large enough to contain a statistically significant number of melt-rich bands.

The number of subvolumes of 20-, 50-, 100-, 200-, and 400-pixel³ size that cover the entire rotated digital sample is \sim 8.5 \times 10⁵, \sim 54,000, 5,503, 585, and 51, respectively (Figure 2a). For the three largest sizes, the transport properties of all the subvolumes that encompass the entire sample were obtained. However, for the two smallest sizes, only a selected subset (\sim 1,170) of subvolumes of each series was analyzed. The selected subvolumes were located at either the uppermost corner or the center of each 200-pixel³ subvolume.

2.4. Melt Distribution Quantification

Melt fraction and melt connectivity were quantified using the modules provided by Avizo 2022.1 (©Thermo-Fisher Scientific) software. Automated subvolume selection and data collection were implemented using our own Python script.

BADER ET AL. 5 of 22

The total melt fraction (ϕ_t) of a subvolume was calculated using the *Volume Fraction* module in Avizo. This module computes the number of voxels of the selected phase divided by the total number of voxels within the subvolume to obtain the total volume fraction of the phase. The total melt fraction is a scalar quantity that does not depend on direction.

We then identify the interconnected melt network using the *Axis Connectivity* module in Avizo. For each melt voxel, this module inspects whether it touches any of its 6-nearest melt voxels and identifies all paths that connect melt voxels between the two opposite sides of a subvolume. The interconnected melt voxels are then assigned to a new phase, differentiating them from the non-connected melt voxels. For example, in Figure 2b, the connected melt pockets along the X direction are highlighted in green, whereas the non-connected melt pockets remain gray. The *Volume Fraction* module can then be used on this new phase to obtain the connected melt fraction (ϕ_c) of the subvolume.

The connected melt fraction depends on the direction linking the sides used to define connection. Figure 2b illustrates that in a 400-pixel³ subvolume, the interconnected melt network along the X-direction (highlighted in green) is different from that along the Z-direction (in blue). In this example, no interconnected network was detected along the Y-direction (all melt voxels remain gray). Because interconnected melt networks are sensitive to direction, we define different connected melt fractions ϕ_c^X , ϕ_c^Y , and ϕ_c^Z along the X-, Y-, and Z-directions. Connected melt fraction also varies with scale. Figure 2b illustrates how, although there is no connected melt path along the Y-direction in the 400-pixel³ subvolume, connected melt paths are detected in the 100-pixel³ subvolume at its upper left corner. Conversely, the tortuous, connected melt paths could be cut off in the smallest subvolumes yet included in the larger subvolumes. Therefore, to accurately quantify the melt network connectivity, the connected melt fraction is measured for every subvolume size as well as in each direction.

2.5. Melt Volume Orientation Measurement Using the Image Moment Method

Melt connectivity and permeability can be affected by the elongation of melt volumes, which may occur in response to stress (Takei & Holtzman, 2009). To evaluate if melt volumes present a consistent orientation throughout the sample, we measure Melt Volume Orientation (MVO) using the *Label Analysis* module provided by *PerGeos 2022.1* (© ThermoFisher Scientific) software. There are several ways to define the orientation of a melt volume. Here, we report the orientation of the major image moment, which indicates the direction along which the melt volume is most concentrated (Figure 3). Unlike other popular methods, such as the determination of a Feret radius or a convex hull, the image moment is less sensitive to rugosity at the surface of the volume and emphasizes instead its bulk, through which most melt flow takes place.

The Moment of Inertia module of PerGeos 2022 provides image moment information. First, the module computes the centroid of an object labeled as a melt volume, which is equivalent to the center of mass for an object of uniform density. Then, the module calculates the inertia matrix $J = \sum_k m_k (||\mathbf{r}_k||^2 \mathbf{I} - \mathbf{r}_k \mathbf{r}'_k)$, where I is the identity matrix, \mathbf{r}_k is the vector joining the centroid and voxel k, m_k is the mass associated with that voxel, and the summation is taken over all the voxels labeled as melt. Finally, the Major Inertia Axis is defined as the eigenvector of the inertia matrix associated with its smallest eigenvalue, that is, the direction along which mass is most concentrated. The major inertia axis is equivalent to a geometrically defined major image moment axis, as the density PerGeos assigns to the melt volume to calculate the moment of inertia is uniform. The volume V_i and elongation E_i , defined as the ratio of largest and smallest moments of inertia, are also reported for each melt volume i.

The orientation of the major inertia axis gives the orientation of a given melt volume *i*. Hence, the MVO is quantified using the azimuth (θ_i) and the pitch (φ_i) of the major inertia axis (Figure 3). The azimuth is the clockwise angle (0–360°) from the *X*-axis in the XY plane, while the pitch is the angle (0–90°) from the *Z*-axis toward the XY plane. Each measurement can be represented as a non-directed axis that intersects a unit sphere once in each hemisphere (Figure 3). To better understand the distribution of axes, we define density contours using a Watson density kernel with self-consistent concentration parameter *C* (see Fisher et al. (1987) and Text S2 in Supporting Information S1). The lower hemisphere contours are presented on an equal-area Schmidt projection with its pole corresponding to the *Z*-axis.

BADER ET AL. 6 of 22

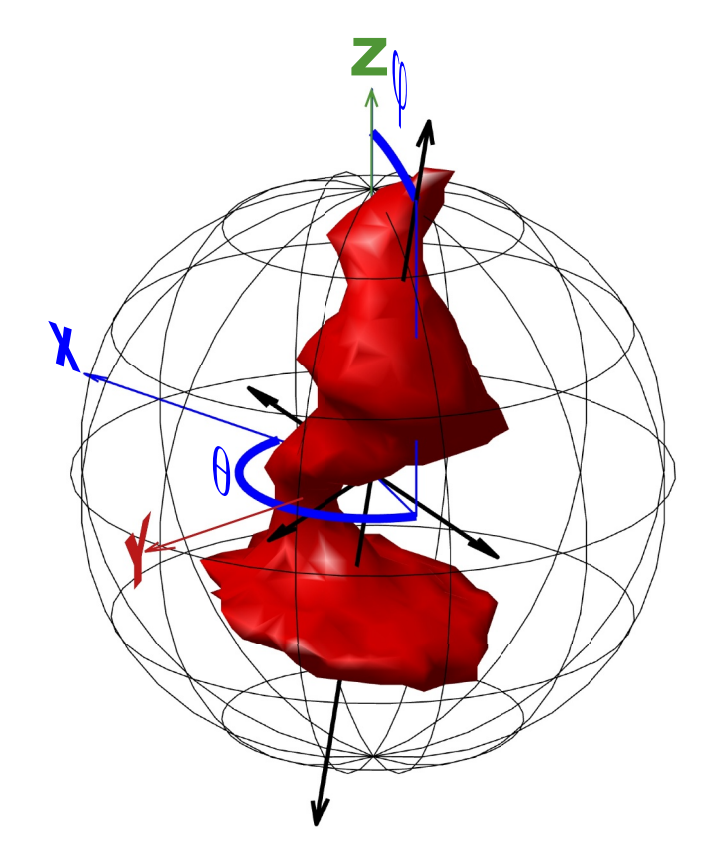


Figure 3. Illustration of the inertia axes (black arrows) associated with a melt volume (red object). The melt volume's centroid (center of mass) serves as the origin of all vectors and the center of the unit sphere shown in this diagram. The moment of inertia tensor represents how mass is concentrated normal to any given direction. It is represented here by its three eigenvectors (black arrows). The longest arrow represents the major moment of inertia axis, which is associated with the smallest eigenvalue of the moment of inertia tensor and, therefore, indicates the direction along which the melt volume is most concentrated. Its orientation is reported using the pitch angle φ and the azimuth angle θ , shown here in blue.

The orientation of a given melt volume i is represented by the orientation matrix

$$T_{i} = \begin{bmatrix} x_{i}x_{i} & x_{i}y_{i} & x_{i}z_{i} \\ y_{i}x_{i} & y_{i}y_{i} & y_{i}z_{i} \\ z_{i}x_{i} & z_{i}y_{i} & z_{i}z_{i} \end{bmatrix},$$
(1)

where $x_i = \cos(\varphi_i) * \cos(\theta_i)$, $y_i = \cos(\varphi_i) * \sin(\theta_i)$, and $z_i = \sin(\varphi_i)$. The orientation matrix is then averaged over the entire data set:

$$T = \frac{\sum_{i} w_i T_i}{\sum_{i} w_i} \,. \tag{2}$$

Here, w_i is a weight associated with each measurement. Unweighted estimates are provided by the special case $w_i = 1$. However, the orientation of the smallest melt volumes is not calculated reliably, due to discretization issues, and may even be associated with an unphysical elongation less than one. To address this issue, we experimented with weights that depend on melt volume or elongation. We also experimented with filtering out all the melt volumes below a certain shape factor or volume, which may be less reliable. All the obtained visualizations are shown in Figures S8–S11 in Supporting Information S1. The unweighted orientations appear concentrated toward the reference frame axes, but these density maxima vanish when the data are weighted using any of the strategies we tried. This suggests that some of the smaller melt volumes are truncated by subvolume edges. Finally, we settled on using $w_i = V_i$, which retains all the information collected but emphasizes the largest melt volumes and minimizes the effects of truncation artifacts.

Following Woodcock (1977) the ranked eigenvalues $\tau_1 < \tau_2 < \tau_3$ of T can be used to characterize the type of MVO distribution with the definition of a shape parameter $\gamma = \log\left(\frac{\tau_3}{\tau_2}\right)/\log\left(\frac{\tau_2}{\tau_1}\right)$ and the strength parameter $\zeta = \log\left(\frac{\tau_3}{\tau_1}\right)$. A polar distribution, where the axes are concentrated toward a specific direction, has $\gamma = \infty$, whereas a girdle-like distribution, in which the axes are

concentrated close to a great circle, or equivalently, perpendicular to the pole of that great circle, has $\gamma=0$, which also corresponds to $\tau_2\approx\tau_3$. Filtering the data has only a small effect on the orientation of the eigenvectors of T, but it changes where on a γ - ζ fabric discriminant diagram the data set plots (Figures S8–S12 in Supporting Information S1). The unweighted data, which are most subjected to artifacts of discretization, appears more bipolar, whereas weighing by melt volume produces MVO fabrics that are the least bipolar (Figure S13 in Supporting Information S1).

MVOs were collected and analyzed for each subvolume size, except for the 400-pixel³, for which the number of melt volumes was often larger than software capabilities. This analysis allows us to determine if melt volumes have a preferred orientation, the nature of the associated shape-preferred orientation (SPO), and if the SPO changes across length-scale.

2.6. Permeability Calculation

We calculate the permeability of each subvolume extracted from the sample, using the *Absolute Permeability lattice Boltzmann method (LBM)* module in *PerGeos 2022.1* (©ThermoFisher Scientific). The LBM determines the probability that a particle with a given momentum occupies a volume element at a given position at any instant based on the interaction between neighboring particles. Figure 4 shows the flow field of a selected 400-pixel³ calculated using the *Absolute Permeability Experimental* Solution in Avizo ©. Flow trajectories conform to the complex geometry of the boundary between melt and solid. The LBM does not solve continuum fluid mechanics

BADER ET AL. 7 of 22

21699356, 2024, 3, Down loaded from https://agupubs.onlinelibrary.wiley.com/doi/10.1029/2023JB028065 by Norwegian Institute Of Public Healt Invo

Figure 4. Flow streamlines in the (a) X- (b) Z- and (c) Y-direction. Disconnected melt is visualized in gray, while the connected melt is shown in green, blue, and red for the X-, Z-, and Y-direction volumes, respectively. In this visualization, streamlines were initiated from the front-facing or top panel using the *Absolute Permeability Experimental Solution* in Avizo ©. Note the X- and Z-directions are similar in their connected flow path (i.e., through the melt-rich band), while the Y-direction has no connected flow path and, therefore, zero permeability over this length scale.

equations but incorporates kinematic rules that represent the physics that govern fluid flow (Bernsdorf et al., 1999). Thus, it captures the overall behavior of the flow (e.g., Chen & Doolen, 1998).

One advantage of the LBM is that, because it is rule-based and only considers local interactions, it can handle complex domain geometries such as the melt-labeled images of our sample. Thus, it has found widespread use in the evaluation of permeability in porous media based on 3-D images, where it appropriately recovers experimentally derived values (Ferréol & Rothman, 1995). Furthermore, the LBM is computationally efficient and parallelizes readily, which makes it an important tool for analyzing fluid transport in high-resolution tomographic images (e.g., Alpak et al., 2018; Bultreys et al., 2016). It would be unfeasible to examine the number of subvolumes we consider in this study using a finite-difference or finite-element-based method.

In this study, we solve fluid flow in the portion of the image labeled as "melt." The LBM preserves the 3D geometric complexity of the melt network. The averaged flow velocity \bar{v}_j in a direction x_j (X-, Y-, or Z-direction) and the pressure gradients in that direction, $\partial p/\partial x_j$, lead to an estimate of the component k_{jj} of the permeability in that direction, thanks to Darcy's relation

$$v_j = -\frac{k_{jj}}{\mu} \frac{\partial p}{\partial x_j},\tag{3}$$

where μ is the viscosity of the fluid flowing through the melt network. The calculation is repeated for flow in the X, Y, and Z directions for every subvolume of every size considered (Figure 4). We evaluate permeability anisotropy by calculating the components of permeability parallel to (X-, Z-directions) and perpendicular to (Y-direction) the preferred MVO. Note that flow is possible only if there is a connected melt network. These calculations help us to understand how the distribution of melt in sample QC0705 influences transport properties at various scales.

3. Results

3.1. Connected Versus Total Melt Fraction

Figure 5 reports the connected melt fractions ϕ_c^x , ϕ_c^y , and ϕ_c^z along the X, Y, and Z directions as a function of the total melt fraction, ϕ_t , of each selected subvolume. The arithmetic average of ϕ_t is 0.074, 0.076, 0.077, 0.076, 0.076 for the 20-, 50-, 100-, 200-, and 400-pixel³ subvolumes, respectively (Table 1). These values are very close to the total melt fraction of the sample (0.078), which indicates that the discretization is representative of the entire sample even considering only a selection of the possible 20- and 50-pixel³ subvolumes is included. However, the range of total melt fraction is scale-dependent. The total melt fraction of the 20-pixel³ subvolumes ranges from 0 (no melt) to more than 0.95 (nearly all melt). This range narrows as the subvolume size increases. For the

BADER ET AL. 8 of 22

.com/doi/10.1029/2023JB028065 by Norwegian Institute Of Public Healt Invoice Receipt DFO, Wiley Online Library on [04/03/2024]. See the Terms and Conditions (https://onlinelibrary.wiley.com/terms

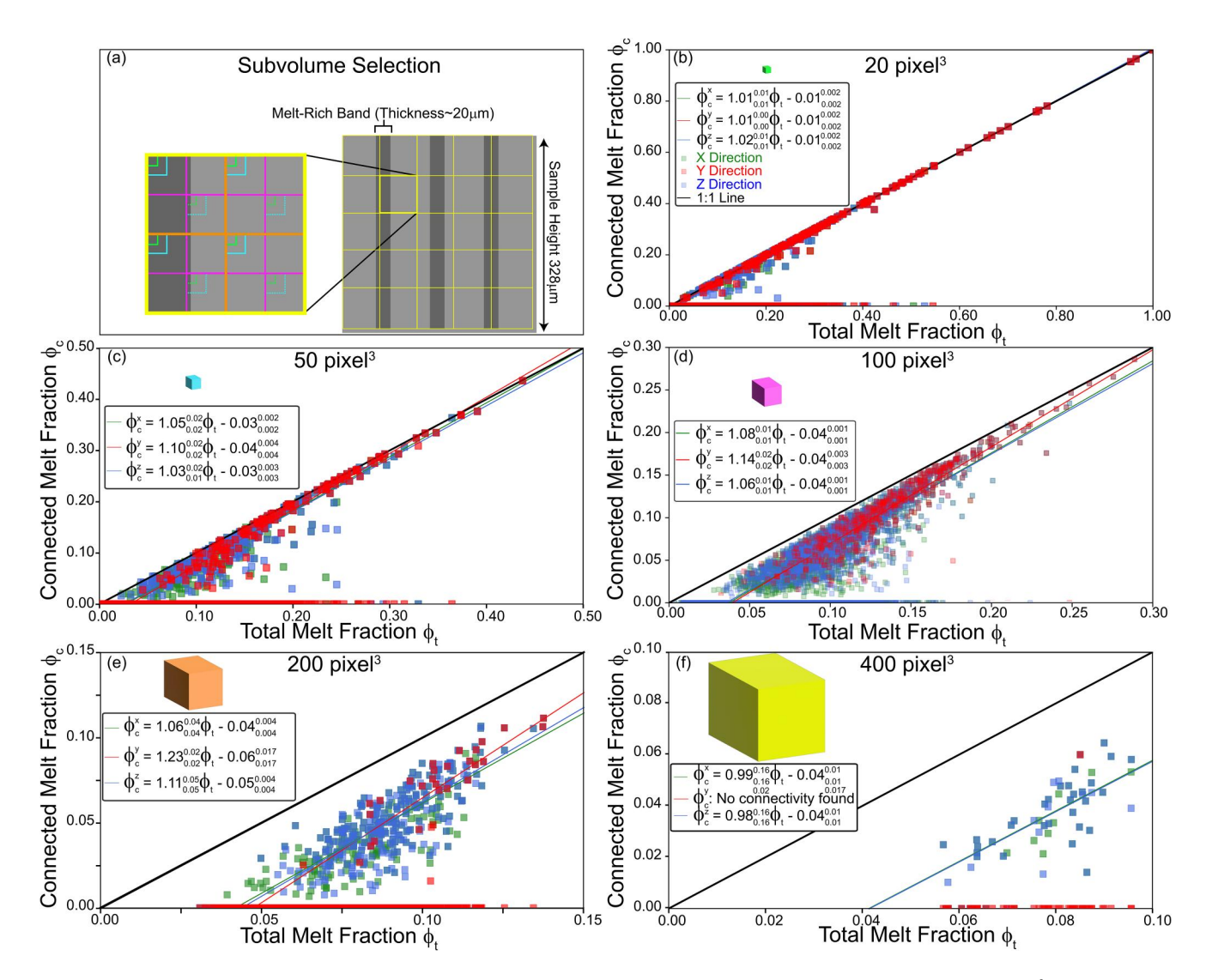


Figure 5. (a) 2-D schematic diagram of subvolume distribution within a digital rock. On the right, the yellow squares represent the 400-pixel³ subvolumes and their relation to melt-rich bands and melt-poor regions (dark and light gray, resp.). The insert on the left shows the positions of the smaller subvolumes of 200-, 100-, 50-, and 20-pixel³ (orange, pink, cyan, and green, resp.) within a representative 400-pixel³ subvolume. Panels (b) through (f) plot the connected melt fractions along X-, Y-, and Z-directions (green, red, and blue squares) vs. the total melt fraction for the (b) 20-, (c) 50-, (d) 100-, (e) 200- and (e) 400-pixel³ subvolumes, with the relative size of the subvolume illustrated as a cube in each panel. The thin green, red, and blue lines correspond to the linear regression of data points with positive connected melt fraction values along the X-, Y-, and Z-direction. The black 1:1 line represents the situation in which all melt voxels are interconnected ($\phi_c = \phi_l$). Note that the range of melt fractions displayed is different in each panel.

400-pixel³, ϕ_t ranges from ~0.055 to ~0.095. The 400-pixel³ are large enough to contain more than one of the melt-rich bands but not a statistically significant number of them. Because each subvolume of this size encompasses different proportions of melt-rich and melt-poor regions, large variations in melt fractions are expected even at the largest subvolume size we consider.

At any given subvolume size, the connected melt fractions ϕ_c^X , ϕ_c^Y , and ϕ_c^Z of a subvolume generally increase linearly with the total melt fraction of the same subvolume (Figure 5):

$$\phi_c^j = a\phi_t + b,\tag{4}$$

where j = X, Y, or Z represents flow direction parallel to the X-, Y-, and Z-axis, respectively. The values of the slope a and intercept b depend on the direction of flow as well as the subvolume size (Table 1, Figure 5). Figure 5b shows that most measurements of connected versus total melt fraction in 20-pixel³ subvolumes are close to the 1:1

BADER ET AL. 9 of 22

Subvolume size	Axial direction	$\phi_{\scriptscriptstyle t}$	$[\tau_1, \tau_2, \tau_3]$	*a	*b	** $\phi_{t,50}$	***n	***C
20-pixel ³ (~1 grain)	X	0.074 ± 0.01	[0.38, 0.36, 0.26]	1.01 ± 0.01	-0.01 ± 0.02	0.14	2.19 ± 0.13	113 ± 22
	Y			1.01 ± 0.00	-0.01 ± 0.02	0.22	2.37 ± 0.18	143 ± 32
	Z			1.02 ± 0.01	-0.01 ± 0.02	0.15	2.36 ± 0.14	113 ± 23
50-pixel ³ (~20 grains)	X	0.076 ± 0.06	[0.42, 0.36, 0.22]	1.05 ± 0.02	-0.03 ± 0.002	0.11	2.44 ± 0.13	71 ± 17
	Y			1.10 ± 0.02	-0.04 ± 0.004	0.19	1.99 ± 0.31	358 ± 157
	Z			1.03 ± 0.02	-0.03 ± 0.003	0.12	2.38 ± 0.15	71 ± 20
100-pixel ³ (~100 grains)	X	0.077 ± 0.04	[0.43, 0.38, 0.19]	1.08 ± 0.01	-0.04 ± 0.001	0.08	2.44 ± 0.08	90 ± 15
	Y			1.14 ± 0.02	-0.04 ± 0.003	0.15	1.81 ± 0.18	$1,133 \pm 349$
	Z			1.06 ± 0.01	-0.04 ± 0.001	0.09	2.71 ± 0.09	45 ± 8
200-pixel ³ (~1,000 grains)	X	0.076 ± 0.02	[0.46, 0.39, 0.15]	1.06 ± 0.04	-0.04 ± 0.004	0.08	3.18 ± 0.26	22 ± 10
	Y			1.23 ± 0.02	-0.06 ± 0.017	0.13	2.10 ± 1.00	1,426 ± 1,284
	Z			1.11 ± 0.05	-0.05 ± 0.004	0.08	3.57 ± 0.34	7 ± 4
400-pixel ³ (~10,000 grains)	X	0.076 ± 0.01	N/A (not measurable)	0.99 ± 0.16	-0.04 ± 0.01	0.06	3.6 ± 1.00	9 ± 8
	Y			N/A	N/A	N/A	N/A	N/A
	Z			0.98 ± 0.16	-0.04 ± 0.01	0.05	4.9 ± 0.90	0.3 ± 0.3

Note. See Section 3.1 for definitions of a, b, and $\phi_{t,50}$, and Section 3.2 for definitions of n, C.

line. In that case, the slope a and the intercept b for all three directions are ~ 1 and ~ 0 , respectively. In other words, most of the melt is connected over length scales of 20 pixels regardless of direction. With increasing subvolume size, the connected melt fraction becomes progressively smaller than the total melt fraction (Figures 5c–5f). As the subvolume size increases from 20- to 200-pixel³, the slope a becomes steeper and the intercept b becomes more negative (Figures 5a–5e, Table 1), suggesting the proportion of disconnected melt increases in larger-sized subvolumes with low ϕ_t regardless of direction. The results for the 400-pixel³ subvolumes do not fit perfectly into these trends (Figures 5f and Table 1). However, the 400-pixel³ data are more scattered, and the uncertainties in the values of both a and b are the largest. The smaller number of 400-pixel³ subvolumes contributes to both the narrower range of melt fraction and the observed scatter (Figure 5a).

Importantly, the melt fractions connected in the X-direction and Z-direction are indistinguishable from each other but have a markedly different relation to melt fraction and subvolume size than melt fraction connected in the Y-direction. The slope a is higher in the Y-direction than in the X- and Z-direction when subvolumes are larger than the grain scale, indicating a larger change in ϕ_c^Y than ϕ_c^X or ϕ_c^Z for a given change in ϕ_t . As detailed below, the proportion of subvolumes with melt connected in the Y-direction decreases with increasing subvolume size, to the point that only one 400-pixel³ has a non-zero ϕ_c^Y . As the 400-pixel³ subvolumes are large enough to encompass both melt-rich bands and the melt-poor regions that separate them, the absence of connectivity in the Y-direction in the largest subvolumes implies that there is essentially no melt flow between individual melt-rich bands.

3.2. Frequency Distribution of Melt Fraction

Figure 6 presents frequency distributions of subvolumes having a given total melt fraction. The frequency distributions are constructed from histograms of total melt fraction with a bin size of 0.01 and are repeated for all subvolume sizes (see Text S3 and Figure S13 in Supporting Information S1 for detailed statistics). The frequency distribution obtained for 20-pixel³ subvolumes is approximately logarithmic (Figure 6a), but becomes peaked for larger subvolume sizes (Figures 6b–6e). The distributions are right-skewed with peaks at \sim 0.03 and \sim 0.05–0.07 for 50-pixel³ and 100-pixel³ subvolumes, respectively (Figures 6b and 6c). The distribution is approximately normal with a peak at \sim 0.07 for 200-pixel³ subvolumes (Figure 6d) and becomes left-skewed with a peak at \sim 0.09 for 400-pixel³ subvolumes (Figure 6e).

At each size, we also calculated the total melt fraction frequency distribution for just the subvolumes that have interconnected melt. Different frequency distributions are associated with subvolumes with $\phi_c^X > 0$, $\phi_c^Y > 0$, or

BADER ET AL. 10 of 22

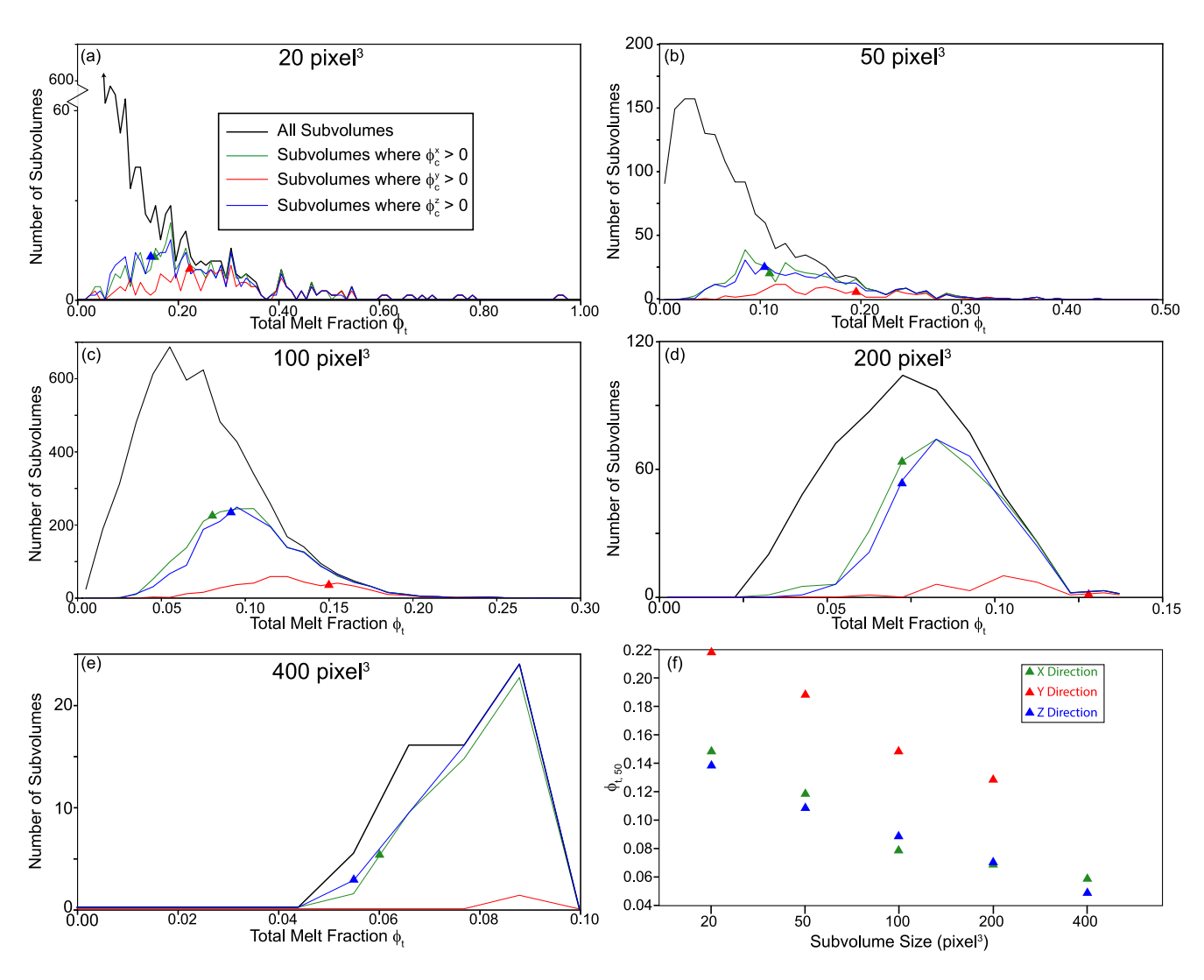


Figure 6. Total melt fractions (ϕ_t) frequency distributions among all subvolumes (black curve), or only the subvolumes with $\phi_c^X > 0$ (green), $\phi_c^Y > 0$ (red), or $\phi_c^Z > 0$ (blue). Each panel corresponds to a subvolume size: (a) 20-, (b) 50-, (c) 100-, (d) 200-, and (e) 400-pixel³. The total melt fraction $\phi_{t,50}$ at which 50% of the subvolumes have $\phi_c^X > 0$, $\phi_c^Y > 0$, or $\phi_c^Z > 0$ is marked as a green, red, or blue triangle on the corresponding curve. (e) Summary of $\phi_{t,50}$ for each direction reported against subvolume size. Note that the range of melt fractions displayed is different in each of panels (a) to (e).

 $\phi_c^Z > 0$ (Figure 6). For all five subvolume sizes, the total melt fraction frequency distributions among subvolumes with melt networks interconnected in the X- and Z-directions are very similar (Figure 6). These frequency distributions appear roughly uniform for 20-pixel³ subvolumes with connected melt (Figure 6a). As the subvolume size increases, these distributions exhibit a peak at a total melt fraction of ~ 0.085 (Figures 6a–6e), close to the melt fraction of the sample as a whole. The corresponding frequency distributions for subvolumes with melt networks interconnected in the Y-direction are very broad with a peak that cannot be confidently evaluated due to noise in the histograms. The number of subvolumes with melt connected in the Y-direction is systematically lower than the number of subvolumes with melt connected in the X or Z-direction at a given melt fraction, regardless of subvolume size.

Figure 6 also demonstrates that, as the subvolume size increases, the proportion of subvolumes with $\phi_c^X > 0$ or $\phi_c^Z > 0$ increases, whereas the proportion of subvolumes with $\phi_c^Y > 0$ decreases. The total melt fraction at which all subvolumes of a given size (100%) have connected melt fractions, $\phi_{t,100}$, decreases with increasing subvolume size. The values of $\phi_{t,100}$ for $\phi_c^Y > 0$ are generally larger than those for $\phi_c^X > 0$ or $\phi_c^Z > 0$ at the same subvolume size.

BADER ET AL. 11 of 22

We also report $\phi_{1.50}$, the total melt fraction at which half of the subvolumes (50%) have non-zero connected melt fractions (Table 1). That melt fraction is shown as colored symbols in Figures 6a-6e and is reported as a function of subvolume size in Figure 6f. If a subvolume size is considerably smaller than the width of melt-rich bands (~125 pixels), only those subvolumes lying entirely within the melt-rich bands (high ϕ_t) have a melt network connected in the directions contained in the melt-rich bands (i.e., in either the X- or the Z-direction). As the subvolume size increases, subvolumes encompassing both melt-rich bands and melt-poor regions (smaller ϕ_t) can also have a melt network connected parallel to the melt-rich bands. Hence, the values of $\phi_{\rm t,50}$ decreases with increasing subvolume size. At all scales, the melt network is less well connected in the Y-direction (normal to the melt-rich bands) than in the X- or Z-direction so that $\phi_{\rm t,50}$ is larger for the Y-direction than for the other two directions (Figure 6f). For the Y-direction, $\phi_{1.50}$ is much larger than the overall melt fraction in the sample, which indicates that connection in that direction occurs dominantly in melt-rich bands. Only one 400-pixel³ subvolume contains interconnected melts in the Y-direction, therefore, $\phi_{1.50}$ is never reached for this direction and scale (Figure 6f). This confirms the earlier inference that there is essentially no melt flow between individual melt-rich bands.

3.3. Melt Volume Orientation

Figure 7 presents on a lower-hemisphere equal-area Schmidt projection density contours of the MVO weighted by melt volume for each subvolume size data set. The contours are generally concentrated at higher density values, which confirms the existence of a real fabric. By contrast, the contours of the unweighted data set shown in Figures S8–S11 in Supporting Information S1 are concentrated to low values, indicating that noise dominate that data set. We also see in the unweighted data set artifacts linked to truncation by the X, Y, and Z directions that define subvolume edges, but these artifacts are minimized in the volume-weighted data set shows in Figure 7.

The highest density contours are centered on the X-Z plan parallel to the melt-rich bands, which indicates that melt volumes are oriented preferentially parallel to the bands at all scales. The eigenvectors associated with the average orientation matrix for each subvolume set are also indicated on each panel and confirm this conclusion. In particular, the eigenvector associated with the smallest orientation eigenvalue plots very close to the Y-axis, confirming that melt volume orientations perpendicular to the plane defined by melt-rich bands are the least likely. The eigenvector associated with the largest eigenvalue of the orientation matrix plots 10°-30° away from the X-axis but always in the X-Z plane, implying some level of heterogeneity within that plane.

The eigenvalues of the orientation matrix are helpful to differentiate between different types of fabric. The discriminant diagram of Figure 8 shows that MVO forms a clear girdle, especially at the largest subvolume sizes. The pole of that girdle is the same as the Y-axis, defined as the axis normal to the melt rich band plane. Thus, melt volumes are preferentially oriented within a plane parallel to melt-rich bands, but do not have a strong alignment within that plane. The intensity of the fabric, indicated by the ζ parameter, increases with increasing size of the subvolumes in the data set, implying more orientation variability at the grain scale (20-pixel³) than close to the band scale (200-pixel³). Unfortunately, it was not possible to collect MVO information at 400-pixel³ scale because the large number of melt volumes within an individual subvolume exceeds software capacity. The increasing large contour values in Figure 7 and τ_1 in Table 1 confirm fabric intensity increases with subvolume size.

3.4. Permeability-Total Melt Fraction Relationship

The permeability along the X-, Y-, and Z-directions, k^{X} , k^{Y} , and k^{Z} , was measured using the Lattice Boltzman Method for all subvolumes and is reported as a function of melt fraction ϕ_1 on Figure 9. At any given subvolume size, some of the subvolumes have zero permeability due to the lack of connected melt networks in our digital rock analogs. However, it is conceivable that connection exists at scales below our image resolution. For completeness, these subvolumes are shown in Figure 9 on each panel with a permeability of 1.78×10^{-18} m², the permeability at the resolution limits of our imaging (see Section 4.1 for a discussion), even though their measured permeability is in fact zero.

The relationship between permeability and total melt fraction can be approximated using a power law (Miller et al., 2014),

BADER ET AL. 12 of 22

21699356, 2024, 3, Downloaded from https://agupubts.onlinelibrary.viley.com/doi/10.1029/2023JB028065 by Norwegian Institute Of Public Healt Invoice Receipt DFO, Wiley Online Library on [0.403/2024]. See the Terms and Conditions (https://onlinelibrary.wiley.com/doi/10.1029/2023JB028065 by Norwegian Institute Of Public Healt Invoice Receipt DFO, Wiley Online Library on [0.403/2024]. See the Terms and Conditions (https://onlinelibrary.wiley.com/doi/10.1029/2023JB028065 by Norwegian Institute Of Public Healt Invoice Receipt DFO, Wiley Online Library on [0.403/2024]. See the Terms and Conditions (https://onlinelibrary.wiley.com/doi/10.1029/2023JB028065 by Norwegian Institute Of Public Healt Invoice Receipt DFO, Wiley Online Library on [0.403/2024]. See the Terms and Conditions (https://onlinelibrary.wiley.com/doi/10.1029/2023JB028065 by Norwegian Institute Of Public Healt Invoice Receipt DFO, Wiley Online Library on [0.403/2024]. See the Terms and Conditions (https://onlinelibrary.wiley.com/doi/10.1029/2023JB028065 by Norwegian Institute Of Public Healt Invoice Receipt DFO, Wiley Online Library on [0.403/2024]. See the Terms and Conditions (https://onlinelibrary.wiley.com/doi/10.1029/2023JB028065 by Norwegian Institute Of Public Healt Invoice Receipt DFO, Wiley Online Library on [0.403/2024]. See the Terms and Conditions (https://onlinelibrary.wiley.com/doi/10.1029/2023JB028065 by Norwegian Institute Of Public Healt Invoice Receipt DFO, Wiley Online Library on [0.403/2024]. See the Terms and Conditions (https://onlinelibrary.wiley.com/doi/10.1029/2023JB028065 by Norwegian Institute Of Public Healt Invoice Receipt DFO, Wiley Online Library on [0.403/2024]. See the Terms and Conditions (https://onlinelibrary.wiley.com/doi/10.1029/2023JB028065 by Norwegian Institute Of Public Healt Invoice Receipt DFO, Wiley Online Library on [0.403/2024]. See the Terms and Condition (https://onlinelibrary.wiley.com/doi/10.1029/2023JB028065 by Norwegian Institute Of Public Receipt DFO, Wiley Online Receipt DFO, Wiley Online Receipt DFO

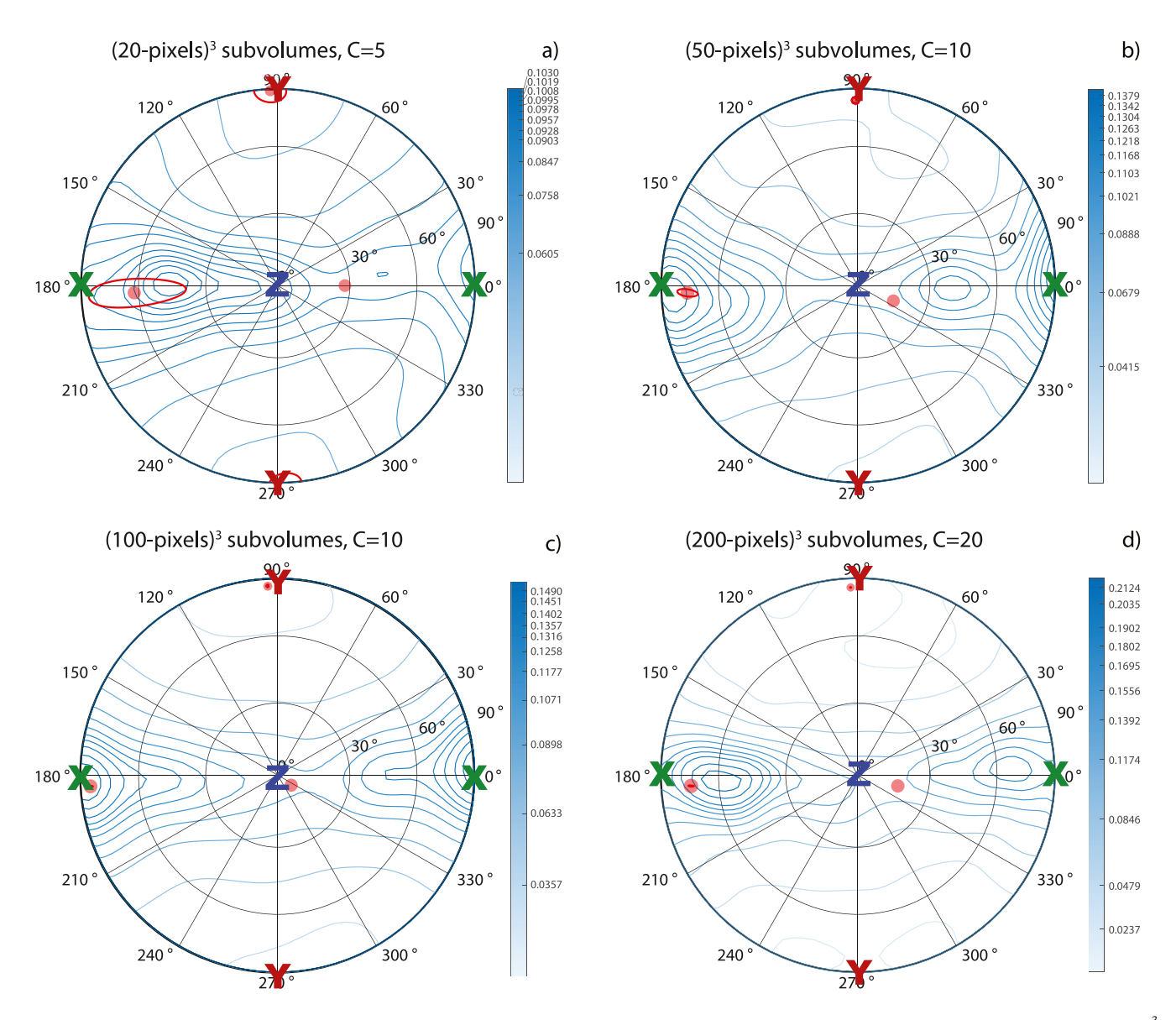


Figure 7. Melt volume orientation (MVO) density contours reported on a lower-hemisphere equal-area Schmidt projection for each subvolume size: (a) 20-pixel³; (b) 50-pixel³; (c) 100-pixel³; (d) 200-pixel³. MVO data are weighted by MVO volume. Each title indicates the concentration factor *C* of the Watson distribution used as density kernel in each case. The eigenvectors of each data set are shown as red circle with uncertainty ellipse. The X-, Y-, and Z-axes are indicated for reference.

$$k^{j} = \frac{\phi_{t}^{n} d^{2}}{C},\tag{5}$$

where the index j = X, Y, or Z represents the flow direction parallel to the X-, Y-, or Z-axis, respectively. For different flow directions and subvolume sizes, the power-law exponent n and the geometrical factor C are expected to be different. To calculate the value of C, we used the average grain size $d \approx 3 \mu m$ (Bader, 2020; Qi et al., 2018). We determined the values of n and C from the linear regressions of the data in Figure 9. For any given subvolume size, the values of the power-law exponent and geometric factor for all three directions are listed in Table 1. The power-law exponents are also reported against subvolume size in Figure 10.

For 20-pixel³ subvolumes, the power-law exponent n is ~ 2.3 , slightly below the value of 2.6 that Miller et al. (2014) reported for texturally equilibrated isotropic samples. This value increases with increasing subvolume size for the X- and Z-direction to 2.4–2.7 at the 100-pixel³ scale, then to > 3 at the 400-pixel³ scale. The power-law exponents from permeability in the X- and Z-directions are always within one standard deviation of

BADER ET AL. 13 of 22

.com/doi/10.1029/2023JB028065 by Norwegian Institute Of Public Healt Invoice Receipt DFO, Wiley Online Library on [04/03/2024]. See the Terms

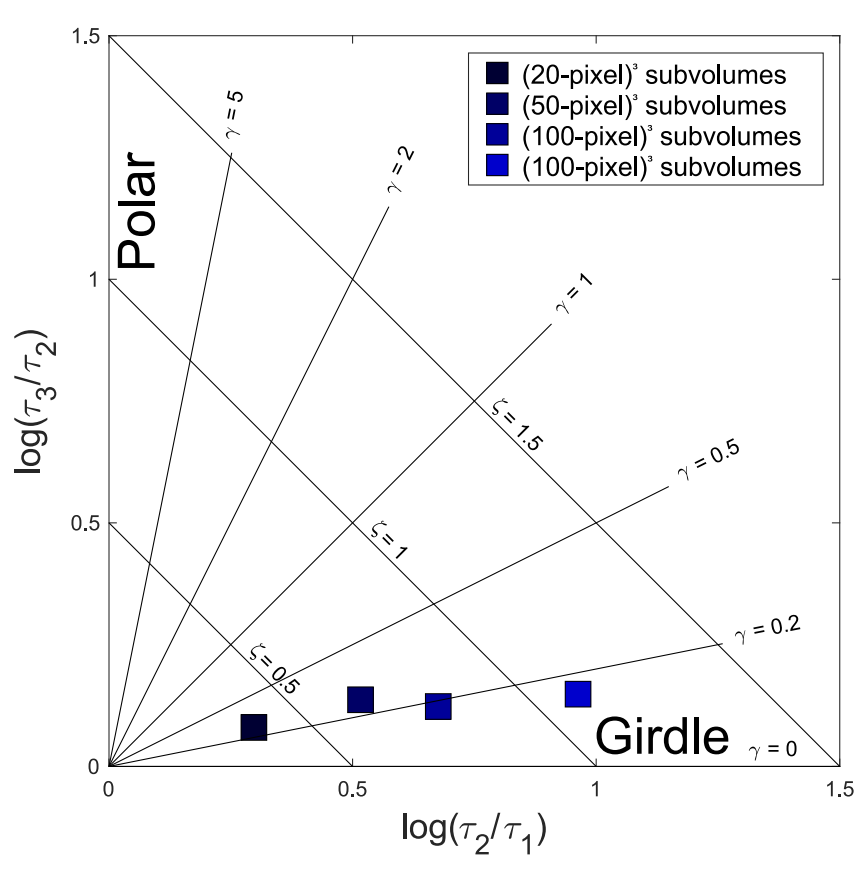


Figure 8. Fabric discriminant diagram for the Melt Volume Orientation distribution presented in Figure 7. The brightness of the symbols increases with subvolume size. The shape parameter $\gamma = \log(\tau_3/\tau_2)/\log(\tau_2/\tau_1)$ indicates the type of fabric, with bipolar fabrics plotting along the vertical axis ($\gamma \to \infty$) and girdle-like distribution plotting along the horizontal axis ($\gamma \to 0$). Fabric intensity increases with the strength parameter $\zeta = \log(\tau_3/\tau_1)$.

each other and increase with increasing subvolume size. In contrast, the power-law exponent in the Y-direction decreases from 2.4 to \sim 1.8 as subvolume size increases from 20- to 100-pixel³. The power-law exponent is poorly constrained above this scale in the Y direction at large subvolume sizes, as few subvolumes have a connected melt network.

4. Discussion

4.1. Robustness of the Results

The largest source of uncertainty in this study results from image processing. Subtle changes in threshold values chosen for different phases may have a considerable impact on melt connectivity and total melt fraction. To address this issue, we compared results using several different image filters and segmentation algorithms. For example, we used the top-hat filter (Miller et al., 2014) in addition to the watershed algorithm to process the microtomographic image (see Text S1 and Figure S3 in Supporting Information S1). We used a closing filter on this segmented data set, connecting melt pockets 10 or fewer pixels apart. These methods produced a somewhat higher total melt fraction (\sim 0.11) than that given in Qi et al. (2018) or presented in the result section.

In Figure S4 in Supporting Information S1, the total melt fraction is plotted against the connected melt fraction for the 100-pixel³ subvolumes of the digital rock created using the top-hat algorithm and closing filter. The connected melt network was also detected using the 26-neighbor method, which could capture connectivity missed by the 6-neighbor method used in the main text. Despite the higher total melt fraction ($\phi_t \approx 0.11$) and more sensitive method for detecting the connected melt network, the relationships between the total and connected melt fraction are quantitatively similar to those in Figure 5d. In addition, the permeability-melt fraction relationship for each direction shown in Figure S5 in Supporting Information S1 are similar to those in Figure 9d. The similarity of the

BADER ET AL. 14 of 22

21699356, 2024, 3, Downloaded from https://agupubs.onlinelibrary.wiley.com/doi/10.1029/20231B02066 by Norwegian Institute Of Public Healt Invoice Receipt DFO, Wiley Online Library on [04/03/2024]. See the Terms and Conditions (https://onlinelibrary.wiley.com/term

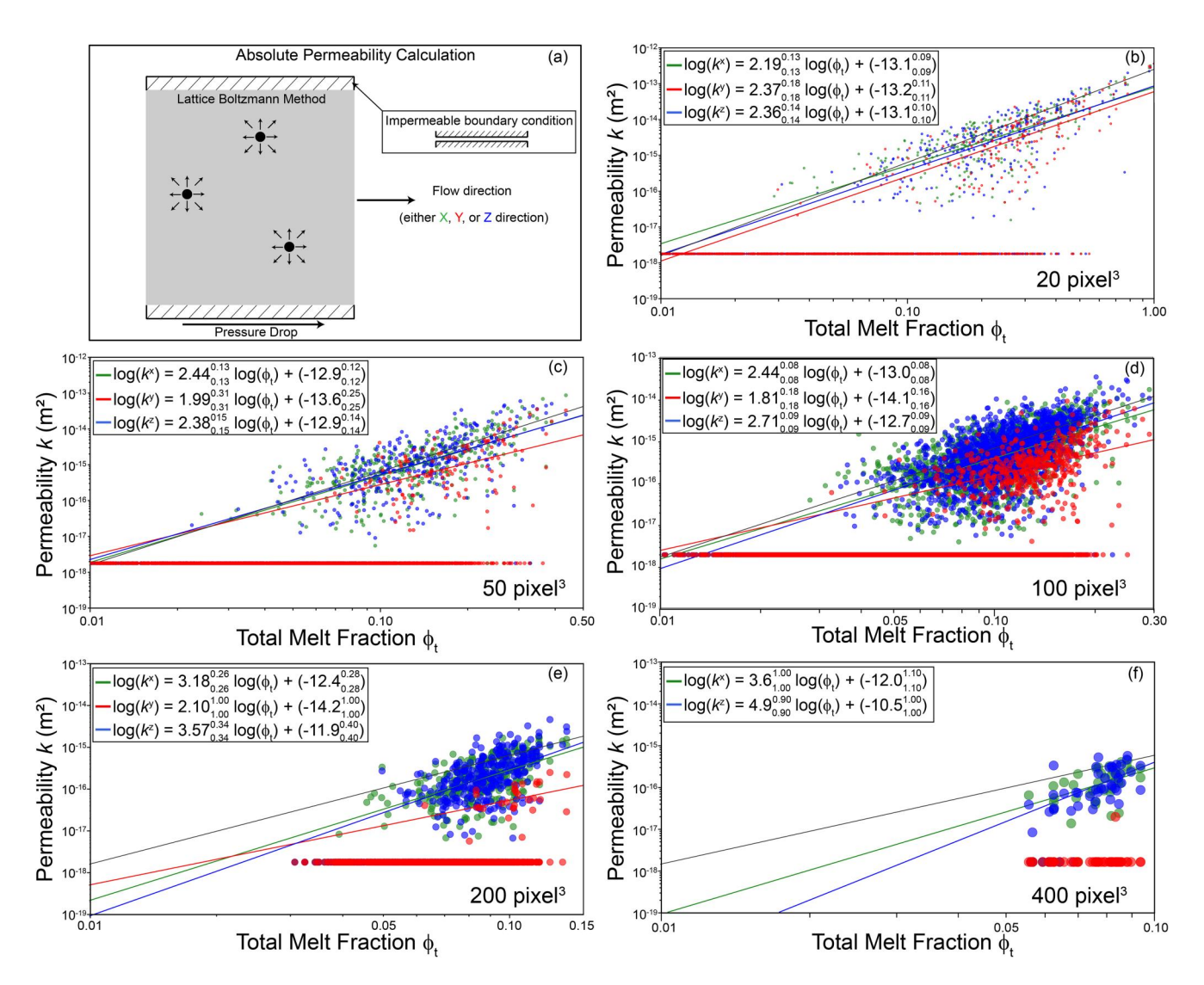


Figure 9. (a) Schematic diagram of the absolute permeability calculation using the Lattice Boltzmann Method, where rules for particle collision (black dots with arrows) are used to solve for fluid flux driven by a pressure drop in one direction. The boundaries of the domain in the other two directions are defined as impermeable. The calculation was repeated for the X-, Y-, and Z-directions. (b-f) Permeability for flow in the X-, Y-, and Z-directions (green, red, and blue circles, respectively) reported vs. total melt fraction (b) 20-, (c) 50-, (d) 100-, (e) 200-, and (f) 400-pixel³ subvolumes, scaled to subvolume size. The thin green, red, and blue lines correspond to the best fit through the data in the X-, Y-, and Z-direction, respectively. Permeability values with no measurement are assigned permeability at the image resolution limit (discussed in Section 4.1). The slope and intercept of each best fit are given on each panel and in Table 1.

quantitative relationships between total melt fraction, connected melt fraction, and permeability suggests that the uncertainty associated with image processing does not seriously affect our results.

If melt network connectivity does exist but was missed by the imaging techniques employed, our melt network connectivity and, therefore, lower-end permeability estimates would change. If the melt tubule throat size were at the image resolution (0.16 µm) of the imaging, we can calculate the permeability using the average grain size of $\sim 3 \,\mu\text{m}$ by assuming a network model of cylindrical tubes along the edges of cubes (Turcotte & Schubert, 2003, p. 428). This calculation yields a permeability of $\sim 1.78 \times 10^{-18} \, \text{m}^2$; this result was included in the permeability values shown in Figure 9. In the following sections, we present and discuss the permeability anisotropy assuming $k^Y = 0$ when no melt connectivity is detected. However, if melt connectivity exists just below the detectability limits, the adjusted k^Y would still be two to more than three orders of magnitude lower compared to the corresponding k^X and k^Z , with higher permeability anisotropy at higher total melt fraction.

To ensure that the observed trends are not sensitive to the location of the discretizing mesh, we also generated a different set of 100-pixel³ subvolumes. The center of each subvolume in the second set is offset by 50 pixels in all

BADER ET AL. 15 of 22



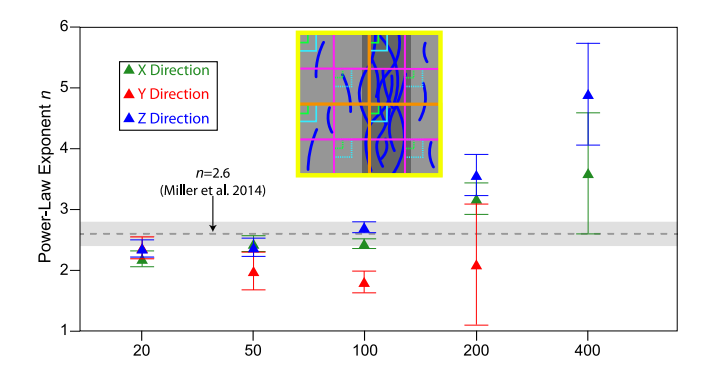


Figure 10. Power-law exponents for the relation between k^X (green triangles), k^Y (red triangles), or k^Z (blue triangles) versus total melt fraction ϕ_t at each subvolume size. The error bar represents one standard deviation. For comparison, the power-law exponent for a texturally equilibrated partially molten olivine-basalt aggregate (Miller et al., 2014) is shown as a dashed line and the gray band represents the uncertainty of that value. The yellow square contains a schematic of a 400–pixel³ subvolume, how it would be subdivided, and the melt network (blue) within the subvolume. The melt network geometry and scale-dependent melt connectivity influence the absolute permeability values and power-law exponents.

three directions from the center of the corresponding subvolume in the original set (Text S1 and Figure S6 in Supporting Information S1). The total and connected melt fractions relationships of the second set (Figure S7 in Supporting Information S1) are statistically indistinguishable from those of the original set, as are the permeability-melt fraction relationships compared to those of the original set.

We quantified MVO using the image moment (specifically, the *Moment of Inertia* module in PerGeos 2022.1) and concluded that at all scales, the MVO is subparallel to the melt-rich bands (Section 3.3). A recent study by Seltzer et al. (2023) reports that individual melt pockets at grain scales are oriented ~25° from the melt-rich band direction. This apparent inconsistency could be due to the higher strain (~13.3) in our sample compared to that studied by Seltzer et al. (2023) (less than 2.5), which may suggest the orientation of individual melt pockets changes progressively with increasing strain. A change of MVO from low to high strain is also observed in Qi et al. (2018). Our analysis also differs from that of Seltzer et al. (2023) in that we used a 3-D image analysis and image moment calculation, not a 2-D image analysis and the longest or shortest path across the melt pockets. Because we focus on the transport properties, the image moment method is more appropriate because it minimizes the influence of dead-ends in the flow path. For example, a long narrow spike on the side of an otherwise straight melt-rich band would have

different effects on the image moment and the PAROR analysis used by Seltzer et al. (2023). While the outline of the melt volume could be strongly influenced by this feature, the image moment dilutes its effect by averaging image information at the same distance from a rotation axis.

4.2. Power-Law Relationship

The power-law exponent n (Equation 1) is related to important characteristics of the melt geometry and can be used to extrapolate permeability to melt fractions beyond those that were measured. The power-law exponents for flow in the X-, Y-, and Z-directions of sample CQ0705 are sensitive to the subvolume size (Figure 10). For the 20-pixel³ subvolumes, the power-law exponents are ~ 2.2 , ~ 2.4 , and ~ 2.4 for k^X , k^Y , and k^Z , respectively (Table 1). Only at this scale is the permeability-total melt fraction exponent for flow normal to the melt-rich bands (Y-direction) comparable to those for flow parallel to the melt-rich bands (X- and Z-directions).

For 50- and 100-pixel³ subvolumes, the power-law exponents for both k^X and k^Z fall between 2.4 and 2.7, a slight increase from those for 20-pixel³ subvolumes. As demonstrated in Figure 10 for 100-pixel³, the values of the power-law exponents for k^X and k^Z fall within 1 standard deviation of the value of n = 2.6 obtained by Miller et al. (2014) for isotropic, textually equilibrated, basalt-olivine aggregates. These power-law exponents increase to more than 3 for the 200- and 400-pixel³ subvolumes. Zhu et al. (1995) determined that, while maintaining the connectivity in a percolation network, the power-law exponent can increase from 2 to 3 as the hydraulic radius becomes more heterogeneous. Loss of connectivity in the percolation network can lead to n > 3 (Bernabé et al., 2003; Zhu et al., 1995; Zhu & Hirth, 2003). As the subvolume size increases beyond 100-pixel³, individual subvolumes include both melt-poor and melt-rich regions. Therefore, parts of their melt networks are poorly connected while others are well-connected, and each subvolume is heterogeneous, which explains the large values of the power-law exponents of these data sets. This result is in contrast to the smaller subvolumes, which have either connected or disconnected melt networks but rarely a mixture of the two. Their more homogeneous melt networks in the smaller subvolumes lead to a power-law exponent near 2.

Interestingly, the exponent for k^{Y} decreases from 2.4 to ~1.8 as the subvolume size increases from 20 to 100 pixel³ (Figure 10). This reduction suggests a slight increase in melt connectivity along the Y-direction as the subvolume size increases from 20 to 100 pixel³, consistent with the connected melt fraction analysis (Figure S13 in Supporting Information S1). Connected melt pathways often meander out of the two smaller-sized subvolumes, limiting the connectivity that can be detected at that scale. Thus, connectivity increases slightly in the Y-direction as the subvolume size increases from 20 to 100 pixel³ as we obtain a more complete picture of the melt network, as illustrated by the schematic in Figure 10. Most 200- and 400-pixel³ subvolumes have little to no interconnected

BADER ET AL. 16 of 22

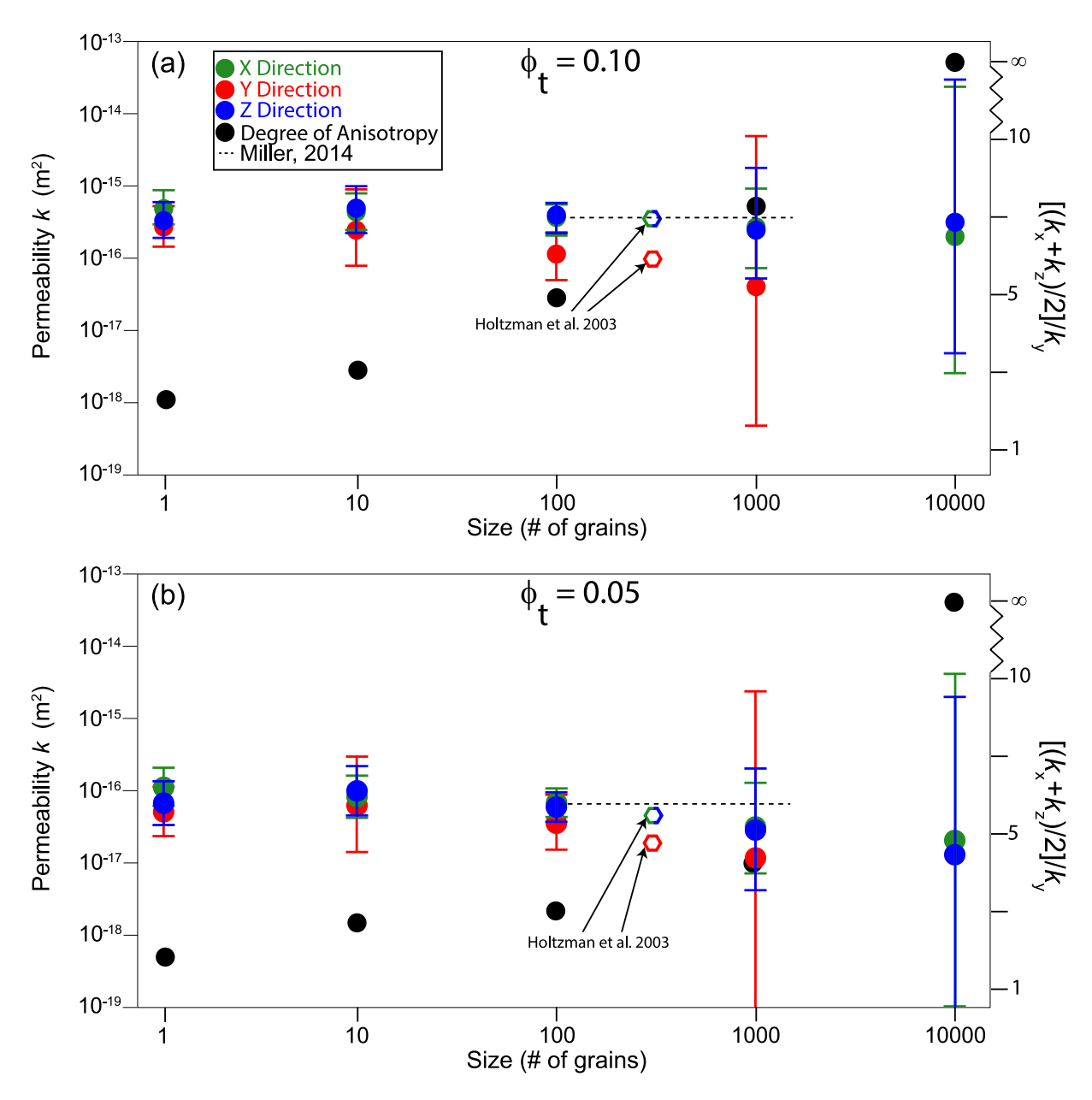


Figure 11. Size dependence of the absolute permeability k^X (green circles), k^Y (red circles), and k^Z (blue circles) of samples having total melt fractions ϕ_t of (a) 0.10 and (b) 0.05, respectively. The error bars represent one standard deviation. The average of permeability parallel to melt band direction over permeability normal to melt band direction, a measure of anisotropy, is reported on the secondary *Y*-axis with black circles. The two open hexagons are permeability estimates of a sheared partially molten rock (Holtzman et al., 2003). The dashed line corresponds to the permeability of an isotropic textually equilibrated partially molten rock (Miller et al., 2014). All the estimates have been recalculated assuming a grain size of 3 μm, to allow for a direct comparison with the results obtained on CQ0705.

melt along the Y-direction, as these subvolumes typically include at least a portion of a melt-poor region between melt-rich bands. The power-law exponents for these cases are poorly (or not) constrained (Figure 10).

4.3. Permeability Anisotropy

From the power-law relationships, we calculated the absolute permeability components k^X , k^Y , and k^Z of subvolumes of various sizes but with total melt fractions ϕ_t of either 0.10 or 0.05 and a grain size of 3 μ m (Figure 11). These melt fractions, which are slightly below and above the sample's average melt fraction of 0.078, provide estimates for permeability in the melt-rich and melt-poor regions of the sheared sample. Note that no values for k^Y were obtained for the 400-pixel³ subvolumes due to the lack of connectivity at this scale normal to the melt-rich

BADER ET AL. 17 of 22

bands (Figure 9f). Holtzman et al. (2003) estimated the permeability in directions parallel (k^X or k^Z) and normal (k^Y) to melt-rich bands using a serial sectioning image technique on a sheared olivine-basalt sample. In this study, we quantified the permeability of a sheared partially molten olivine-basalt at five different length scales. Despite the difference in experimental setup, the estimates of Holtzman et al. (2003) parallel to the melt-rich bands compare favorably with our estimates, while they predict higher permeability normal to melt-rich bands (Figure 11). For reference, we also plotted permeability values of isotropic, texturally equilibrated partially molten rocks with the same total melt fractions (Miller et al., 2014) in Figure 11. To compare these permeability values to ours, we use a grain size d of 3 μ m (Bader, 2020; Qi et al., 2018). We also plot the average calculated permeability, k^X and k^Z , divided by k^Y on the secondary vertical axis in Figure 11 to represent the degree of anisotropy. A value of one is perfectly isotropic, with increasing values for higher anisotropy.

At a total melt fraction of 0.10 (higher than the average total melt fraction of \sim 0.08 therefore representing a meltrich band), k^X and k^Z , are comparable across all subvolume sizes, indicating isotropic flow within the planar meltrich band. While k^Y is very similar to k^X and k^Z in 20-pixel³ subvolumes, it decreases with increasing subvolume size. The anisotropy observed for the 50- and 100-pixel³ subvolumes is likely a result of the tortuous melt flow normal to the melt band direction, where melt meanders through a connected path that is oriented primarily along the X- and Z-directions (Figure 10). This anisotropic behavior is likely caused by the identified SPO of the small-scale melt pockets. Hier-Majumder (2011) proposed that a melt pocket orientation could result in permeability anisotropy of a factor of \sim 10, in the same order but larger than the value that we obtained at the scale of 10–100 grains. Interestingly, the degree of anisotropy we obtained is close to, but slightly below, the range predicted by numerical models that attempt to explain the low-angle of melt-rich bands (Taylor-West & Katz, 2015).

Because the thickness of melt-rich bands is $\sim 20~\mu m$ (i.e., $\sim 125~pixels$, $\sim 7~grains$), the 200- and 400-pixel³ subvolumes containing melt-rich bands must also include some melt-poor regions. The drastic reduction of k^Y in the two largest subvolumes sizes (Figure 11a) suggests melt transport becomes increasingly difficult in the melt-poor regions normal to the melt-rich bands. The resulting permeability anisotropy, of a factor of $\sim 10~or$ greater for the 400-pixel³ subvolume, is primarily a result of a lack of melt connectivity along the Y-direction. This anisotropy is higher than predicted by just the development of melt pocket orientation (Hier-Majumder, 2011) and higher than previously measured for a sheared olivine-basalt using serial sectioning (Holtzman et al., 2003). At the largest subvolume scale considered here, permeability anisotropy is extreme and allows no flow perpendicular to the plane of melt-rich bands. Such anisotropy could limit the efficiency of melt segregation, which may explain the higher fraction of melt left in between melt-rich bands in experiments than in models of stress-induced melt segregation in which permeability anisotropy remains finite (e.g., Katz et al., 2006).

These observations are reinforced by the permeability data at a total melt fraction of 0.05. The permeability k^{Y} of the 400-pixel³ subvolumes at this melt fraction, which is lower than the average total melt fraction of ~0.08, is zero due to the lack of melt connectivity along the Y-direction. It is clear that, in the melt-poor region of a sheared partially molten rock, no melt flow occurs between the melt-rich bands.

Overall, Figure 11 demonstrates that, for melt flow parallel to the melt-rich bands, the permeability of a sheared partially molten rock is insensitive to subvolume size and is comparable to that of an isotropic, texturally equilibrated partially molten rock. The permeability values are comparable even though melt flow is localized and takes place only in the connected melt network. The permeability of subvolumes larger than 20-pixel³ is anisotropic, with the anisotropy increasing strongly as the subvolume size increases. While the intermediate-scale anisotropy seems directly caused by the melt-volume orientation, the large-scale anisotropy is a result of reduced melt connectivity. Over large length scales, flow is completely anisotropic and uniplanar. Melt flow takes place exclusively along the melt band direction.

4.4. Relation Between Melt Geometry and Permeability and the Evolution of Melt-Rich Bands

The statistics of MVO provide a microphysical basis to understand the scale-dependent characteristics of permeability discussed earlier. Melt Volume Orientation is distributed along a uniaxial girdle with its pole in the Y-direction, which explains permeability anisotropy. As the melt volumes are rarely elongated along the Y-direction, transport in that direction must follow a tortuous path dominated by segments oriented parallel to melt-rich bands with only an occasional deviation out of that plane. This behavior leads to the kind of anisotropy that we document in Figure 11. Furthermore, the increase in MVO fabric intensity with increasing scale explains

BADER ET AL. 18 of 22

the increasingly dominant permeability anisotropy to the point where flow at sample scale takes place exclusively parallel to the melt-rich band planes.

We could identify no preferred flow direction within the plane of the melt-rich bands, further supported by the girdle-plane distribution found for the MVO and the similarity in melt connectivity for the X- and Z-direction. The slight deviation from an axisymmetric girdle in Figures 7 and 8 may reflect the shearing direction within melt-rich bands, but we have no means of independently confirming this suggestion. For melt flow normal to the melt-rich bands, the permeability decreases with increasing subvolume size.

Importantly, some level of flow perpendicular to the melt bands must be present if, as laboratory experiments suggest, the angle between melt-rich bands and the shear plane does not depend on strain. If no such flow exists, melt would remain confined to the melt bands proper, which are then sheared passively as part of the sample. At the strain of 13 experienced by our sample, no passively sheared plane can deviate by more than 5° from the shear plane, whereas an angle of 20°-30° is seen in experiments (Holtzman et al., 2003; King et al., 2010). Butler (2012) and Taylor-West and Katz (2015) argued that bands with the proper orientation form when melt pockets are aligned with the direction of maximum compression, which would be $\sim 20^{\circ}$ from the melt-rich band plane. In contrast to small strain experiments (e.g., Takei, 2010), Zimmerman et al. (1999) found that melt pockets make an angle of 20° from the maximum compression direction in olivine-basalt aggregates deformed to a strain of 2. It is quite possible that MVO has different properties at small and large strains, perhaps as a result of the development of melt-rich bands. Melt bands may form under conditions for which melt volumes are elongated toward the maximum compression direction (Butler, 2012; Katz et al., 2006; Rees Jones et al., 2020), but their later evolution may be influenced by the kind of uniplanar flow and MVO anisotropy we describe here. Flow perpendicular to the plane of melt-rich bands appears limited at high strain. Dedicated theoretical analyses are necessary to conclude if band-normal flow at the scale of a few grains is sufficient to maintain band orientation or if bands take advantage and "scavenge" the residual melt trapped between melt-rich bands.

4.5. Geological Implications

This study provides the first systematic quantification of permeability, melt connectivity, and three-dimensional melt orientation in a deformed partially molten rock containing discrete melt-rich bands. Our results suggest that, in regions in which stress-driven melt-rich bands form, permeability anisotropy over large length scales could be much more pronounced than previously predicted. This observation could have important implications on melt focusing toward mid-ocean ridges. For example, a recent model by Rees Jones et al. (2020) suggests that melt-rich bands are orientated sub-vertically toward the base of the lithosphere. In this case, we expect melt to ascend and pool along the base of the lithosphere, with very little melt flow parallel to it, because of the lack of large-scale melt connectivity perpendicular to the melt-rich bands. This mode of melt migration is compatible with permeability barrier models (e.g., Sparks & Parmentier, 1991) in which melt flows toward the ridge axis following the topography of the base of the lithosphere (Hebert & Montési, 2010). Some flow normal to the melt-rich bands could be possible if bands form an anastomosing network as seen in some experimental studies (e.g., Kohlstedt & Holtzman, 2009). Nonetheless, melt flow is strongly concentrated along the melt-rich band direction as evidenced by our results.

Another form of melt localization, the reaction infiltration instability (Aharonov et al., 1995; Pec et al., 2017, 2020; Spiegelman et al., 2001) is expected to dominate over stress-driven melt localization throughout most of the mid-ocean ridge melting regime, though both operate together in many regions (Rees Jones et al., 2020). While King et al. (2011) suggested that melt-rich regions produced by a combination of stress and reaction have a similar morphology to those produced by shear alone, the properties we measure here have yet to be examined for melt channels produced by RIIs or by a combination of stress and reaction.

The strong anisotropy in permeability observed in this study may help to better understand the U-series and trace element disequilibrium observed in mid-ocean ridge basalts and abyssal peridotites (Jull et al., 2002; Liu & Liang, 2019; Lundstrom, 2000). For example, a recent modeling study of localized melt flow resulting from reaction and shear suggested that the U-series disequilibrium is best reproduced if the permeability is strongly anisotropic (Liu & Liang, 2019). Given the extreme anisotropy we find as a result of reduced melt connectivity and emerging uniplanar flow, such models could benefit from including texturally driven permeability anisotropy, as opposed to anisotropy solely as a result of melt fraction variation. However, further work is needed to

BADER ET AL. 19 of 22

determine if our results are valid across a range of strains, or if the relationships reported here are valid for localized melt flow induced by RIIs or by both RIIs and stress.

We recognize that CQ0705 was deformed to a large strain (i.e., 13.3), at a higher strain rate and smaller grain size than is likely achieved in the mantle. However, Holtzman et al. (2003) suggested that melt-rich band morphology evolves into a dynamic equilibrium by a strain of ~1. At dynamic equilibrium, the melt-rich band morphology itself does not change significantly with increasing strain, although melt-rich bands may become thicker and farther apart (Holtzman & Kohlstedt, 2007). Based on the difference in strain, strain rate, and grain size among experiments, Holtzman et al. (2003) proposed that melt-rich bands of the kind observed in sample CQ0705 could be centimeters to meters wide and spaced meters to kilometers apart in the mantle. Butler (2009) proposed the accumulated strain in these regions would be ~4, well above the strain needed for melt-rich bands to develop. Thus, our inference of uniplanar flow with a permeability similar to that of isotropic rocks, but with severely restricted flow perpendicular to the plane of melt-rich bands, should be generally applicable to the conditions encountered in mid-ocean ridges. A combination of 3D imaging and digital rock physics models provide a novel approach to quantify physical properties, including transport properties presented in this study, electrical conductivity (e.g., Miller et al., 2015) and seismic wave velocity (e.g., Lyakhovsky et al., 2021). Quantitative constraints of these properties will allow better interpretations of geophysical observations of the upper mantle.

5. Conclusion

We quantified the effect of stress-driven melt localization on melt orientation, melt connectivity, and rock permeability based on high-resolution 3-D microtomographic images of a sheared partially molten rock. The melt orientation, total melt fraction, connected melt fraction, and permeability were obtained at five different length scales using a digital rock physics approach. Our data indicate that the range of total melt fraction varies with length scale. At the smallest scale studied (equivalent to the average grain size), melt pockets are interconnected both parallel and normal to the planar melt-rich bands, and their orientations are more uniformly distributed. At this scale, the permeability is nearly isotropic. As the size of the subvolume increases, melt pockets become disconnected normal to the melt-rich bands, whereas an interconnected melt network persists parallel to the meltrich band direction, along which melt is oriented. The permeability of large subvolumes is completely anisotropic. Parallel to the melt-rich bands, the relationship between permeability and total melt fraction can be approximated by a power-law function with a power-law exponent between 2.2 and 4.9, depending on the length scale. The permeability is comparable to that of an isotropic, textually equilibrated partially molten rock with the same melt fraction. This observation holds even though melt flow is localized, occurring only in regions where the melt forms a connected network. This result suggests that the rate of melt transport along melt-rich bands is comparable to that in an isotropic porous network. Normal to the melt-rich band, however, the absolute permeability decreases with increasing length scale, seemingly related to melt pocket orientation and melt connectivity. Little to no melt connectivity exists between melt-rich bands in our sample. These results provide the first experimental constraints on melt transport anisotropy via shear-induced flow using reliable three-dimensional imaging techniques.

Data Availability Statement

Data is available in the OSF repository (Bader et al. (2024). The MVO fabric code is available on GitHub (Montési et al., 2024). The repository includes the script used to collect subvolumes and associated data, the subvolumes themselves, the segmented rotated synchrotron microtomography data set, and the spreadsheets of data collected from the segmented images using the script provided. For help implementing the script, interested readers are encouraged to contact the corresponding author.

References

Aharonov, E., Whitehead, J. A., Kelemen, P. B., & Spiegelman, M. (1995). Channeling instability of upwelling melt in the mantle. *Journal of Geophysical Research: Solid Earth*, 100(B10), 20433–20450. https://doi.org/10.1029/95JB01307

Alpak, F. O., Gray, F., Saxena, N., Dietderich, J., Hofmann, R., & Berg, S. (2018). A distributed parallel multiple-relaxation-time lattice Boltzmann method on general-purpose graphics processing units for the rapid and scalable computation of absolute permeability from high-resolution 3D micro-CT images. Computational Geosciences, 22(3), 815–832. https://doi.org/10.1007/s10596-018-9727-7

Bader, J. A. (2020). Characterizing 3-dimensional melt distribution and anisotropic permeability in sheared partially molten rocks. Digital Repository at University of Maryland. https://doi.org/10.13016/rcfw-slmc

Acknowledgments

Partial support from the National Science Foundation, under Grant EAR-1761912, EAR-2154072, and EAR-2218314, and the National Aeronautics and Space Administration, under Grant 80NSSC20K0465, is acknowledged. We thank T. Tamarkin for preparing the specimen for the microtomography experiments. We thank Richard Katz for suggesting the addition of the MVO data, and thank Matej Pec for his discussion of preliminary melt pocket orientation data. Comments from Laurent Arbaret and an anonymous reviewer helped improve the manuscript.

BADER ET AL. 20 of 22

- Bader, J. A., Zhu, W., & Montesi, L. (2024). QC0705, OSF [Dataset]. https://doi.org/10.17605/OSF.IO/YJB3E
- Bernabé, Y., Mok, U., & Evans, B. (2003). Permeability-porosity relationships in rocks subjected to various evolution processes. Pure and Applied Geophysics, 160(5), 937–960. https://doi.org/10.1007/PL00012574
- Bernsdorf, J., Durst, F., & Schäfer, M. (1999). Comparison of cellular automata and finite volume techniques for simulation of incompressible flows in complex geometries. *International Journal for Numerical Methods in Fluids*, 29(3), 251–264. https://doi.org/10.1002/(SICI)1097-0363(19990215)29:3<251::AID-FLD783>3.0.CO;2-L
- Bultreys, T., De Boever, W., & Cnudde, V. (2016). Imaging and image-based fluid transport modeling at the pore scale in geological materials: A practical introduction to the current state-of-the-art. Earth-Science Reviews, 155, 93–128. https://doi.org/10.1016/j.earscirev.2016.02.001
- Butler, S. L. (2009). The effects of buoyancy on shear-induced melt bands in a compacting porous medium. *Physics of the Earth and Planetary Interiors*, 173(1), 51–59. https://doi.org/10.1016/j.pepi.2008.10.022
- Butler, S. L. (2012). Numerical models of shear-induced melt band formation with anisotropic matrix viscosity. *Physics of the Earth and Planetary Interiors*, 200–201, 28–36. https://doi.org/10.1016/j.pepi.2012.03.011
- Chen, S., & Doolen, G. D. (1998). Lattice Boltzmann method for fluid flows. Annual Review of Fluid Mechanics, 30(1), 329–364. https://doi.org/10.1146/annurev.fluid.30.1.329
- Cmíral, M., Gerald, J. D. F., Faul, U. H., & Green, D. H. (1998). A close look at dihedral angles and melt geometry in olivine-basalt aggregates: A TEM study. Contributions to Mineralogy and Petrology, 130(3), 336–345. https://doi.org/10.1007/s004100050369
- Connolly, J., W Schmidt, M., Solferino, G., & Bagdassarov, N. (2009). Permeability of asthenospheric mantle and melt extraction rates at mid-ocean ridges. *Nature*, 462(7270), 209–212. https://doi.org/10.1038/nature08517
- Ferréol, B., & Rothman, D. H. (1995). Lattice-Boltzmann simulations of flow through Fontainebleau sandstone. *Transport in Porous Media*, 20(1–2), 3–20. https://doi.org/10.1007/BF00616923
- Fisher, N. I., Lewis, T., & Embleton, B. J. (1987). Statistical analysis of spherical data (p. 329). Cambridge University Press.
- Hebert, L. B., & Montési, L. G. J. (2010). Generation of permeability barriers during melt extraction at mid-ocean ridges. Geochemistry, Geophysics, Geosystems, 11(12). https://doi.org/10.1029/2010GC003270
- Hier-Majumder, S. (2011). Development of anisotropic mobility during two-phase flow. *Geophysical Journal International*, 186(1), 59–68. https://doi.org/10.1111/j.1365-246X.2011.05024.x
- Holtzman, B. K., Groebner, N. J., Zimmerman, M. E., Ginsberg, S. B., & Kohlstedt, D. L. (2003). Stress-driven melt segregation in partially molten rocks. Geochemistry, Geophysics, Geosystems, 4(5). https://doi.org/10.1029/2001GC000258
- Holtzman, B. K., & Kohlstedt, D. L. (2007). Stress-driven melt segregation and strain partitioning in partially molten rocks: Effects of stress and strain. *Journal of Petrology*, 48(12), 2379–2406. https://doi.org/10.1093/petrology/egm065
- Jull, M., Kelemen, P. B., & Sims, K. (2002). Consequences of diffuse and channelled porous melt migration on uranium series disequilibria. Geochimica et Cosmochimica Acta. 66(23), 4133–4148. https://doi.org/10.1016/S0016-7037(02)00984-5
- Katz, R. F., Jones, D. W. R., Rudge, J. F., & Keller, T. (2022). Physics of melt extraction from the mantle: Speed and style. Annual Review of Earth and Planetary Sciences, 50(1), 507–540. https://doi.org/10.1146/annurev-earth-032320-083704
- Katz, R. F., Spiegelman, M., & Holtzman, B. (2006). The dynamics of melt and shear localization in partially molten aggregates. *Nature*, 442(7103), 676–679. https://doi.org/10.1038/nature05039
- King, D. S. H., Holtzman, B. K., & Kohlstedt, D. L. (2011). An experimental investigation of the interactions between reaction-driven and stress-driven melt segregation: 1. Application to mantle melt extraction. *Geochemistry, Geophysics, Geosystems*, 12(12). https://doi.org/10.1029/2011GC003684
- King, D. S. H., Zimmerman, M. E., & Kohlstedt, D. L. (2010). Stress-driven melt segregation in partially molten olivine-rich rocks deformed in torsion. *Journal of Petrology*, 51(1–2), 21–42. https://doi.org/10.1093/petrology/egp062
- Kohlstedt, D. L., & Holtzman, B. K. (2009). Shearing melt out of the Earth: An experimentalist's perspective on the influence of deformation on melt extraction. *Annual Review of Earth and Planetary Sciences*, 37(1), 561–593. https://doi.org/10.1146/annurev.earth.031208.100104
- Liu, B., & Liang, Y. (2019). Importance of permeability and deep channel network on the distribution of melt, fractionation of REE in abyssal peridotites, and U-series disequilibria in basalts beneath mid-ocean ridges: A numerical study using a 2D double-porosity model. *Earth and Planetary Science Letters*, 528, 115788. https://doi.org/10.1016/j.epsl.2019.115788
- Lundstrom, C. (2000). Models of U-series disequilibria generation in MORB: The effects of two scales of melt porosity. *Physics of the Earth and Planetary Interiors*, 121(3), 189–204. https://doi.org/10.1016/S0031-9201(00)00168-0
- Lyakhovsky, V., Shalev, E., Kurzon, I., Zhu, W., Montesi, L., & Shapiro, N. (2021). Effective Seismic wave velocities and attenuation in partially molten rocks. Earth and Planetary Science Letters, 572, 117117. https://doi.org/10.1016/j.epsl.2021.117117
- Miller, K. J., Montési, L. G. J., & Zhu, W. (2015). Estimates of olivine–basaltic melt electrical conductivity using a digital rock physics approach. Earth and Planetary Science Letters, 432, 332–341. https://doi.org/10.1016/j.epsl.2015.10.004
- Miller, K. J., Zhu, W., Montési, L. G. J., & Gaetani, G. A. (2014). Experimental quantification of permeability of partially molten mantle rock. Earth and Planetary Science Letters, 388, 273–282. https://doi.org/10.1016/j.epsl.2013.12.003
- Miller, K. J., Zhu, W., Montési, L. G. J., Gaetani, G. A., Le Roux, V., & Xiao, X. (2016). Experimental evidence for melt partitioning between olivine and orthopyroxene in partially molten harzburgite. *Journal of Geophysical Research: Solid Earth*, 121(8), 5776–5793. https://doi.org/ 10.1002/2016JB013122
- Mirone, A., Brun, E., Gouillart, E., Tafforeau, P., & Kieffer, J. (2014). The PyHST2 hybrid distributed code for high speed tomographic reconstruction with iterative reconstruction and a priori knowledge capabilities. *Nuclear Instruments and Methods in Physics Research Section B: Beam Interactions with Materials and Atoms*, 324(1), 41–48. https://doi.org/10.1016/j.nimb.2013.09.030
- Montesi, L., Bader, J., & Zhu, W. (2024). MVOfabric [Software]. Zenodo. https://doi.org/10.5281/zenodo.10493811
- Ohser, J., & Schladitz, K. (2009). 3D images of material structures Processing and analysis (p. 341). Wiley-VCH Publishing.
- Pec, M., Holtzman, B. K., Zimmerman, M. E., & Kohlstedt, D. L. (2017). Reaction infiltration instabilities in mantle rocks: An experimental investigation. *Journal of Petrology*, 58(5), 979–1003. https://doi.org/10.1093/petrology/egx043
- Pec, M., Holtzman, B. K., Zimmerman, M. E., & Kohlstedt, D. L. (2020). Influence of lithology on reactive melt flow channelization. *Geochemistry, Geophysics, Geosystems*, 21(8), e2020GC008937. https://doi.org/10.1029/2020GC008937
- Qi, C., Hansen, L. N., Wallis, D., Holtzman, B. K., & Kohlstedt, D. L. (2018). Crystallographic preferred orientation of olivine in sheared partially molten rocks: The source of the "a-c switch", Geochemistry, Geophysics, Geosystems, 19(2), 316–336. https://doi.org/10.1002/2017GC007309
- Qi, C., & Kohlstedt, D. L. (2018). Influence of compaction length on radial melt segregation in torsionally deformed partially molten rocks. Geochemistry, Geophysics, Geosystems, 19(11), 4400–4419. https://doi.org/10.1029/2018GC007715
- Qi, C., Kohlstedt, D. L., Katz, R. F., & Takei, Y. (2015). Experimental test of the viscous anisotropy hypothesis for partially molten rocks. Proceedings of the National Academy of Sciences, 112(41), 12616–12620. https://doi.org/10.1073/pnas.1513790112

BADER ET AL. 21 of 22

- Rees Jones, D. W. R., Zhang, H., & Katz, R. F. (2020). Combined analysis of reactive and shear-driven instabilities at mid-ocean ridges. ArXiv:2008.13674 [Physics]. Retrieved from http://arxiv.org/abs/2008.13674
- Riley, G. N., & Kohlstedt, D. L. (1991). Kinetics of melt migration in upper mantle-type rocks. Earth and Planetary Science Letters, 105(4), 500–521. https://doi.org/10.1016/0012-821X(91)90188-N
- Seltzer, C., Peč, M., Zimmerman, M. E., & Kohlstedt, D. L. (2023). Melt network reorientation and crystallographic preferred orientation development in sheared partially molten rocks. *Geochemistry, Geophysics, Geosystems*, 24(9), e2023GC010927. https://doi.org/10.1029/ 2023GC010927
- Sparks, D. W., & Parmentier, E. M. (1991). Melt extraction from the mantle beneath spreading centers. Earth and Planetary Science Letters, 105(4), 368–377. https://doi.org/10.1016/0012-821X(91)90178-K
- Spiegelman, M., Kelemen, P. B., & Aharonov, E. (2001). Causes and consequences of flow organization during melt transport: The reaction infiltration instability in compactible media. *Journal of Geophysical Research: Solid Earth*, 106(B2), 2061–2077. https://doi.org/10.1029/ 2000IB900240
- Stevenson, D. J. (1989). Spontaneous small-scale melt segregation in partial melts undergoing deformation. Geophysical Research Letters, 16(9), 1067–1070. https://doi.org/10.1029/GL016i009p01067
- Takei, Y. (2010). Stress-induced anisotropy of partially moltn rock analogue deformed under quasi-static loading test. *Journal of Geophysical Research: Solid Earth*, 115(B3). https://doi.org/10.1029/2009JE006568
- Takei, Y., & Holtzman, B. K. (2009). Viscous constitutive relations of solid-liquid composites in terms of grain boundary contiguity: 2.
 Compositional model for small melt fractions. Journal of Geophysical Research: Solid Earth. 114(B6), https://doi.org/10.1029/2008JB005851
- Takei, Y., & Holtzman, B. K. (2009a). Viscous constitutive relations of solid-liquid composites in terms of grain boundary contiguity: 1. Grain boundary diffusion control model. *Journal of Geophysical Research: Solid Earth*, 114(B6). https://doi.org/10.1029/2008JB005850
- Takei, Y., & Holtzman, B. K. (2009b). Viscous constitutive relations of solid-liquid composites in terms of grain boundary contiguity: 3. Causes and consequences of viscous anisotropy. *Journal of Geophysical Research*, 114(B6). https://doi.org/10.1029/2008JB005852
- Taylor-West, J., & Katz, R. F. (2015). Melt-preferred orientation, anisotropic permeability and melt-band formation in a deforming, partially molten aggregate. Geophysical Journal International, 203(2), 1253–1262. https://doi.org/10.1093/gji/ggv372
- Turcotte, D. L., & Schubert, G. (2003). Geodynamics. Cambridge University Press.
- von Bargen, N., & Waff, H. S. (1986). Permabilities, interfacial areas and curvatures of partially molten systems: Results of numerical computations of equilibrium microstructures. *Journal of Geophysical Research: Solid Earth*, 91(B9), 9261–9276. https://doi.org/10.1029/JB091jB09n09261
- Waff, H. S., & Bulau, J. R. (1979). Equilibrium fluid distribution in an ultramafic partial melt under hydrostatic stress conditions. *Journal of Geophysical Research: Solid Earth*, 84(B11), 6109–6114. https://doi.org/10.1029/JB084iB11p06109
- Wark, D. A., & Watson, E. B. (1998). Grain-scale permeabilities of texturally equilibrated, monomineralic rocks. Earth and Planetary Science Letters, 164(3), 591–605. https://doi.org/10.1016/S0012-821X(98)00252-0
- Weickert, J. (1999). Coherence-enhancing diffusion filtering. International Journal of Computer Vision, 31(2), 111–127. https://doi.org/10.1023/A:1008009714131
- Woodcock, N. H. (1977). Specification of fabric shapes using an eigenvalue method. Geological Society of America Bulletin, 88(9), 1231–1236. https://doi.org/10.1130/0016-7606(1977)88<1231:SOFSUA>2.0.CO;2
- Zhu, W., David, C., & Wong, T. (1995). Network modeling of permeability evolution during cementation and hot isostatic pressing. *Journal of Geophysical Research: Solid Earth*, 100(B8), 15451–15464. https://doi.org/10.1029/95JB00958
- Zhu, W., Gaetani, G. A., Fusseis, F., Montesi, L. G. J., & De Carlo, F. (2011). Microtomography of partially molten rocks: Three-dimensional melt distribution in mantle peridotite. Science, 332(6025), 88–91. https://doi.org/10.1126/science.1202221
- Zhu, W., & Hirth, G. (2003). A network model for permeability in partially molten rocks. Earth and Planetary Science Letters, 212(3), 407–416. https://doi.org/10.1016/S0012-821X(03)00264-4
- Zimmerman, M. E., Zhang, S., Kohlstedt, D. L., & Karato, S. (1999). Melt distribution in mantle rocks deformed in shear. Geophysical Research Letters, 26(10), 1505–1508. https://doi.org/10.1029/1999GL900259

References From the Supporting Information

- Andrä, H., Combaret, N., Dvorkin, J., Glatt, E., Han, J., Kabel, M., et al. (2013). Digital rock physics benchmarks—Part I: Imaging and segmentation. Computers & Geosciences, 50, 25–32. https://doi.org/10.1016/j.cageo.2012.09.005
- Andrä, H., Combaret, N., Dvorkin, J., Glatt, E., Han, J., Kabel, M., et al. (2015). Digital rock physics benchmarks—Part II: Computing effective properties. *Computers & Geosciences*, 50, 33–43. https://doi.org/10.1016/j.cageo.2012.09.008

BADER ET AL. 22 of 22